Defense Threat Reduction Agency
8725 John J. Kingman Road, MS
6201 Fort Belvoir, VA 22060-6201

DTRA-TR-20-35

TECHNICAL REPORT

Radiation Effects in Diamond Substrates and Transistors

This report is UNCLASSIFIED.

May 2020

HDTRA1-17-1-0007

Prepared by: Aristos Christou,
University of Maryland
College Park, MD 20742

REPORT DOCUMENTATION PAGE

Form Approved
OMB No. 0704-0188

1. REPORT DATE *(DD-MM-YYYY)*	2. REPORT TYPE	3. DATES COVERED *(From - To)*
04/28/2020	2019 Final Report	Jan1 2017-December 31 2019

4. TITLE AND SUBTITLE
RADIATION EFFECTS IN DIAMOND SUBSTRATES AND TRANSISTORS

5a. CONTRACT NUMBER

5b. GRANT NUMBER
HDTRA1-17-1-0007

5c. PROGRAM ELEMENT NUMBER

6. AUTHOR(S)
CHRISTOU, ARISTOS

5d. PROJECT NUMBER

5e. TASK NUMBER

5f. WORK UNIT NUMBER

7. PERFORMING ORGANIZATION NAME(S) AND ADDRESS(ES)
University of Maryland
Materials Science and Engineering Department
College Park, MD 20742-2115

8. PERFORMING ORGANIZATION REPORT NUMBER

9. SPONSORING/MONITORING AGENCY NAME(S) AND ADDRESS(ES)
Defense Threat Reduction Agency
8725 John J. Kingman Road
Fort Belvoir, VA 22060-6201

10. SPONSOR/MONITOR'S ACRONYM(S)
DTRA

11. SPONSOR/MONITOR'S REPORT NUMBER(S)

12. DISTRIBUTION/AVAILABILITY STATEMENT
Unlimited Distribution

13. SUPPLEMENTARY NOTES
None

14. ABSTRACT
Field effect transistors (FET) based on diamond have 2- dimensional hole gas (2DHG) as the conduction channel. In terms of usability in harsh environment, an important aspect of diamond based FETs is its promise of radiation hardness. Two different types of radiation were used. A cyclotron was used for proton irradiation on diamond substrates, and a high capacity dry cell, panoramic gamma irradiator with 60Co as source material was used for gamma irradiation on diamond-based FETs. Diamond substrates were irradiated with protons at 152 keV and fluence of 1012 particles/cm2. Diamond-based devices show promise of radiation-hardness, owing to high binding energy of carbon atoms. However, the two preval

15. SUBJECT TERMS
Radiation effects, gamma, cyclotron accelerator, diamond, field effect transistors, delta doped diamond, hydrogen termination, high hole mobility transistors.

16. SECURITY CLASSIFICATION OF:			17. LIMITATION OF ABSTRACT	18. NUMBER OF PAGES	19a. NAME OF RESPONSIBLE PERSON
a. REPORT	b. ABSTRACT	c. THIS PAGE			Calkin, Jacob A CIV R and D (USA)
Unclassified	Unclassified	Unclassified		80	19b. TELEPHONE NUMBER *(Include area code)* 703-767-5870

FINAL REPORT:
RADIATION EFFECTS IN DIAMOND SUBSTRATES AND TRANSISTORS

Defense Threat Reduction Agency under Grant No. HDTRA1-17-1-0007.

PI. Professor Aris Christou
University of Maryland
College Park, MD 20742

Summary/Abstract
Field effect transistors (FET) based on diamond have 2- dimensional hole gas (2DHG) as the conduction channel. In terms of usability in harsh environment, an important aspect of diamond based FETs is its promise of radiation hardness. Two different types of radiation were used. A cyclotron was used for proton irradiation on diamond substrates, and a high capacity dry cell, panoramic gamma irradiator with 60Co as source material was used for gamma irradiation on diamond-based FETs. Diamond substrates were irradiated with protons at 152 keV and fluence of 10^{12} particles/cm^2. Diamond-based devices show promise of radiation-hardness, owing to high binding energy of carbon atoms. However, the two prevalent types of diamond substrates, (1) H-terminated, and (2) delta-doped, which utilize 2D conduction channel may be susceptible to radiation damage. This work explores gamma radiation tolerance of H-terminated diamond-based field effect transistors (FETs) at low dose irradiation i.e. ≤ 100 kRad and high dose irradiation up to 26.3 MRad. Slight decrease in output characteristics was observed for low dose irradiation. In contrast, a significant increase in drain current output, like that of an annealing effect, was observed for high dose irradiation. Also, bare H-terminated and delta-doped samples' tolerance to 152 keV proton irradiation with 1.03×10^{12} cm^{-2} fluence was tested using Hall measurements. Both samples exhibited increased resistivities, and decreased mobilities and carrier concentrations post-irradiation. The activation energies for conductivity changed due to disruption of trap states and/or formation of new trap states.

Introduction

Diamond transistors with surface 2D conduction channels are projected to be radiation hard with respect to neutrons. However, ionizing radiation hardness may be a problem due to the disruption of the 2D hole concentration. In this paper, the processing of three terminal devices with 2D surface conducting channels is presented as well as analysis of device transfer characteristics. The fabrication technology, surface preparation and testing, radiation induced defects and device characteristics of microwave power field effect transistors (FET) are reviewed. Devices built on 1) high quality diamond surfaces exploiting the 2 dimensional surface conductivity, and 2) the surface two dimensional "hydrogen terminated" conduction layer in diamond single crystals grown by CVD are analysed. The emphasis is on the fundamental physics of radiation effects on two dimensional conduction layers in diamond materials. This is an unexplored area which could lead to new breakthroughs in the performance of high power microwave transistors in extreme environments such as high temperature and high radiation fields.

A very critical application for diamond is the area of power electronics. Single crystal diamond is projected to enable advanced semiconductor switches capable of operating at extremely high power and frequency [1]. Diamond exhibits ideal properties for such applications, including a 5.5 eV bandgap, >10 MV/cm breakdown strength, theoretical electron and hole mobilities exceeding 3800 cm^2 /V*sec, and an outstanding 22 W/cm·K thermal conductivity. However, achieving useful carrier densities in diamond is problematic, as typical dopants (boron, phosphorous) have activation energies exceeding 0.37 eV, leading to low activation efficiencies [2]. This limitation can be overcome by exploiting hole conductivity along 2D conducting channels to fabricate operational field effect transistors (FETs). Experimental 2D conducting channels can be created through hydrogen termination of diamond surfaces, or through delta-doping of diamond epitaxial layers. Hydrogen termination is achieved by exposing extremely clean diamond surfaces to a hydrogen plasma, creating a surface C-H dipole layer that significantly reduces the carrier ionization energy. Adsorbed species, such as atmospheric H_2O or NO_2, or high electron affinity oxides contact this dipole layer, and together generate a near-surface two-dimensional hole gas (2DHG) with carrier densities 10^{12}-10^{14} holes/cm^2 [3]. Incorporation of heavily-doped boron delta layers into intrinsic diamond epitaxial layers can also be used to create 2D conducting channels with high hole density and mobility [4]. Both schemes can be used to fabricate diamond FETs, as shown schematically in Fig. 1.

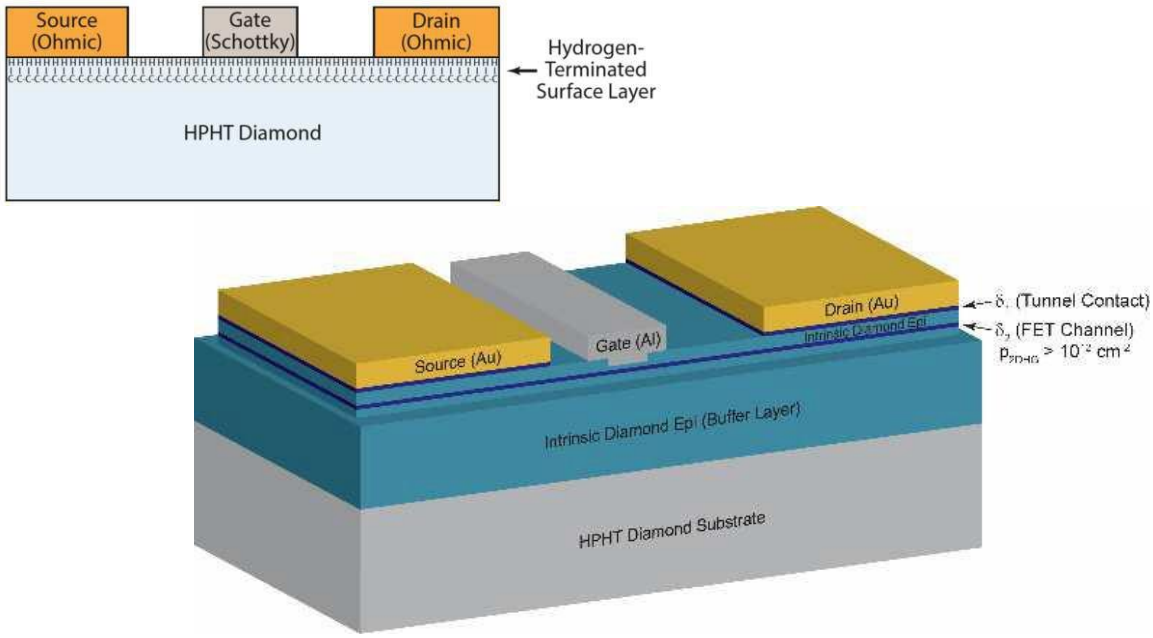

Fig. 1. Diamond FET architectures with 2D hole conduction channels based on (a) hydrogen surface termination and (b) boron delta-doped layers.

Final Results and Discussion

The details of the transistor fabrication and testing are all included in the appendix of this final report. Summarized in the appendix are details for hydrogen terminated FETs as well as the delta doped diamond field effect transistors.

In this final report, we present an over view of the fabrication, characterization, and optimization of diamond FETs with hydrogen-terminated or boron delta-doped 2D hole channels. Single crystal diamond substrates grown by high pressure high temperature (HPHT) synthesis have been prepared to produce ultra-smooth diamond surfaces, shown in Fig. 2, prior to hydrogen termination or chemical vapor deposition (CVD) epitaxy of boron delta layers. These substrates and epilayers were characterized using techniques such as atomic force microscopy (AFM), x-ray photoelectron spectroscopy (XPS), and Fourier-Transform Infrared Spectroscopy (FTIR). The details are also included in the appendix of this annual report. Fabrication and characterization methods are presented and discussed for devices with each 2D conducting channel type. In the case of hydrogen-terminated FETs, multiple processing routes for generation of the 2DHG have been compared, including simple atmospheric adsorbates, intentional NO_2 adsorption, and passivation with high electron affinity dielectrics such as Al_2O_3 and V_2O_5 deposited by atomic layer deposition (ALD). CVD growth techniques for creating boron delta layers used in the delta-doped FETs will also be discussed. Devices have been characterized using transistor current-voltage (as shown in Fig. 3),

capacitance-voltage, and Hall effect measurements, and basic reliability assessments of the various device structures are reported.

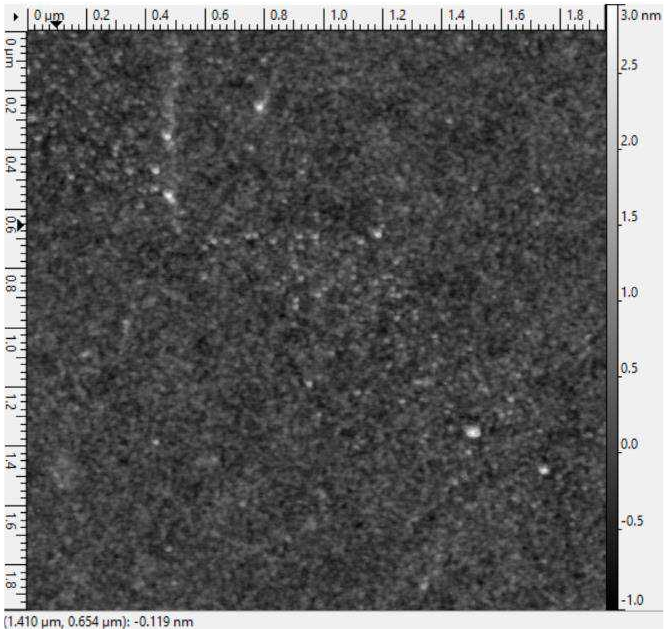

Fig. 2. AFM image of smooth diamond surface, exhibiting 2-3 Å surface roughness. (a) (b)

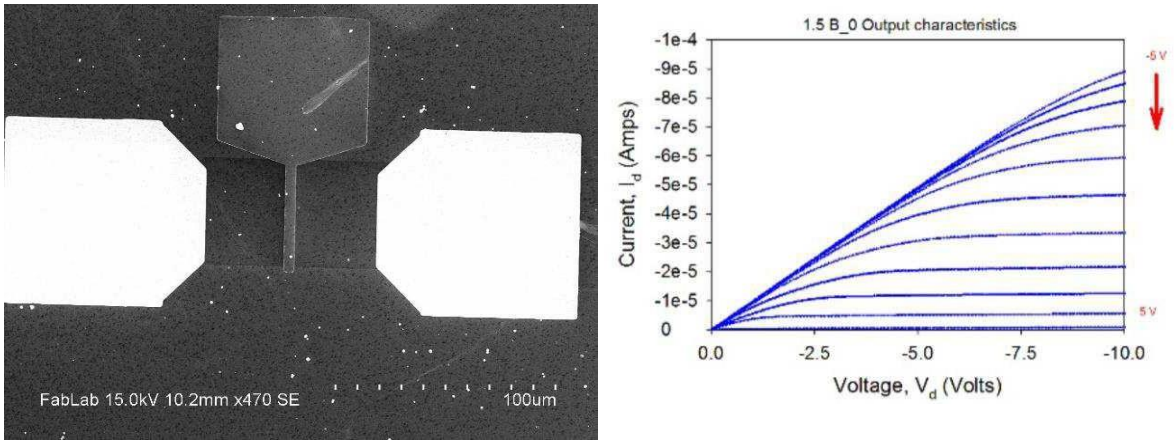

(a) (b)

Fig. 3. (a) Scanning electron microscope image and (b) output characteristics of a hydrogen-terminated diamond FET with Al_2O_3 passivation.

The FETs were subjected to gamma radiation (total dose) and the other devices were subjected to proton irradiation. The delta doped FET fabrication followed the same fabrication steps as the H-terminated FETs. The gate metallization applied was Aluminum and the ohmic contacts were Cr/Au. The fabrication steps were also repeated for the van der Pauw pattern used for mobility measurements. Mobility measurements were also carried out before and after irradiation. The results for the proton irradiation experiments are summarized in Tables 1 and 2 for both mobility changes as well as the comparison of the max drain current at a 5V gate voltage.

Table 1. Proton irradiation on hydrogen terminated diamond FETs

Property	*Pre-Irradiation*	*Post-Irradiation*
Activation Energy (eV)	0.760	0.407
Resistivity (ohm-cm)	8.21×10^{3}	2.65×10^{5}
Mobility (cm^2/V-s)	128.3	6.49
Carrier Concentration (cm^{-2})	2.97×10^{11}	1.79×10^{11}
Max Drain Current at 5V Gate voltage (mA/mm)	695	95.15

Table 2. Proton Irradiation on Delta-Doped FETs

Property	*Double Delta Doped, Pre-Irradiation*	*Double Delta Doped, Post Irradiation*	*Single Delta Doped Pre-Irradiation*	*Single Delta Doped Post Irradiation*
Activation Energy (eV)	0.760	0.407	0.050	0535
Resistivity (ohm-cm)	8.21×10^{3}	2.65×10^{5}	8.45×10^{4}	1.33×10^{1}
Mobility (cm^2/V-s)	128.3	6.49	292	164
Carrier Concentration (cm^{-2})	2.97×10^{11}	1.79×10^{11}	1.28×10^{13}	1.31×10^{12}
Max Drain Current at 5V Gate voltage (mA/mm)	695	95.15	20.87	13.15

Final Project Conclusions

Due to high thermal conductivity, mechanical robustness and ultra-wide bandgap, diamond shows great promise as material for high frequency, high-power device ap- plications. Also, due to high binding energy of carbon atoms in diamond, it is predicted to be radiation hard. Radiation hardness would allow diamond based sensors and devices to be used in harsh environments such as outer-space, nuclear reactors, and the Large Hadron Collider, etc. This work explored radiation hardness of diamond from device point of view.

As such, the diamonds tested had conducting channel activated much below the ultra wide bandgap energy of diamond. This was possible in two ways: (1) terminating HPHT diamond surface with hydrogen, and (2) incorporating heavily boron doped delta layer tens of nanometers underneath the top surface.
FETs were fabricated on H-terminated substrates. Blanket Au layer was deposited, then patterened into mesas, and subjected to O_2 plasma to remove H-termination, isolating the devices. More patterning was done to form Ohmic contacts. Finally, gate dielectric, Al_2O_3, was deposited by ALD, followed by e-beam and liftoff processes to deposit Al gate on top. The FETs were subjected to gamma irradiation from a total dose of 1 kRad to 26.3 MRad. At low dose up to 100 kRad, the FETs showed slight decrease in drain current output, threshold voltage, and maximum transconductance. This could be due to the formation of defects which act as scattering centers. However, vacancies formed Campbell and Mainwood's simulation shows that very few i.e. ≤ 0.09 vacancies/gamma per cm are formed in diamond by gamma irradiation of 1 and 2 MeV [18]. Thus, further research is necessary to determine the cause. In contrast, after high dose ≥ 13.6 MRad gamma irradiation, the drain current output increased sigificantly. Gamma irradiation can form trap states by introducing defects, which could result in enhanced hoping con- ductivity that is responsible for higher output drain current. However, threshold voltage also increased significantly, while gate leakage current remained unchanged. Radiation hardness of diamond was also evaluated for proton irradiation. A cyclotron was used to bombard the samples with 152 keV protons at fluence of $1.03 \times 10^{12}\ cm^{-2}$. This time, bare substrates of H-terminated and delta-doped diamond were used. Hall measurements using the Van der Pauw configuration were performed to evaluate changes in transport properties. Diamond substrates were too small, however, for the available Hall measurement system, HMS-5000, to probe them directly. An alternative approach was designed to get around this size limitation. Insulating pieces of SiO_2 substrate were patterned with Cr/Au contact pads in the corners.

The small diamond substrates also with Cr/Au contact pads in the corners were glued to these bigger SiO_2 substrate using LOR7B resist. This was followed by wire-bonding to join Cr/Au pads on the diamond substrates with Cr/Au pads on the SiO_2 substrates The probes were dropped on the Cr/Au pads on the SiO_2 substrate to perform Hall measurements on the diamond glued to it. Appropriate input current was selected for each substrate before and after proton irradiation to ensure measurements in linear I-V region. At 300 K, H- terminated diamond showed resistivity of $8.21 \times 10^3\ \Omega - cm$, carrier concentration of $2.97 \times 10^{11}\ cm^{-2}$, and hall mobility of $128.3\ cm^2 V^{-1} s^{-1}$. Conduction by p-type carriers and activation energy of 0.76 eV was obtained. Also, mobility increased with temperature closely matching the relationship with temperature of $\mu\ \alpha\ T^2$, which is widely accepted to be due to ionized impurity scattering. After proton irradiation, Hall measurements showed significant differences. At 300 K, sheet resistivity increased to $2.69 \times 10^5\ \Omega - cm$, carrier concentration decreased to $1.8 \times 10^{11}\ cm^{-2}$, and mobility also decreased to $6.49\ cm^2 V^{-1} s^{-1}$. Hall coefficient showed fluctuation between positive and negative sign, indicating mixed carrier conduction. Activation energy decreased to 0.407 eV, indicating formation of a new trap level due to proton irradiation.

Likewise, for delta-doped diamond, resistivity of $8.37 \times 10^4\ \Omega - cm$, carrier concentration of $1.27 \times 10^{12}\ cm^{-2}$, and mobility of $2.92\ cm^2 V^{-1} s^{-1}$ was obtained at 300 K. Hall coefficients again showed mixed carrier conduction. Activation energy of 94.7 meV was obtained, which is close to the expected activation energy for hopping conduction reported by Inushima et al [22]. After proton irradiation, at 300 K, resistivity increased to $1.33 \times 10^5\ \Omega - cm$, sheet carrier concentration was the same at $1.27 \times 10^{12}\ cm^{-2}$, and mobility decreased to $1.84\ cm^2 V^{-1} s^{-1}$. Hall coefficients indicated mixed carrier conduction. Activation energy increased significantly to 0.356 eV, which is close to the boron acceptor level, indicating disruption of the shallow trap state. Simulation of drain current versus source voltage shows degradation of current output by more than an order of magnitude for H-terminated diamond post-proton irradiation. Similarly, for delta-doped diamond, drain current output decreases by less than 40% after proton-irradiation.

The results for the proton irradiation show significant changes in mobility which can be translated to device degradation. Maximum drain current is reduced and hence device transconductance also occurs. This represents the first results for proton irradiation of delta doped diamond devices. The analysis of the mobility results shows that mobility is dominated by ionized impurity scattering. The analysis of the data and the rational for the conclusion are summarized in the appendix.

Future Directions

Based on the results of this work, several topics can be investigated to con- tinue the advancement of knowledge in diamond based devices. A more robust and reliable contact scheme must be developed for reliable measurements of diamond FETs as well as for Hall measurements. This can be done through alloyed contact processing for different metal combinations. To do this as well as measure contact resistance, and sheet resistivity, circular transfer length method (CTLM) pattern has already been prepared to be patterned using electron-beam direct write pro- cedure. Because hydrogen termination is unstable at high temperatures, surface coverage of diamond with hydrogen should be mapped for the entire surface using Micro-Raman spectroscopy. This would also be useful to monitor homogeniety of H-terminated samples, which is crucial for accuracy of Hall coefficient calculation. To ensure less variability, Hall measurements can be performed using Hall bar configuration fabricated at a scale of about 100 microns. Finally, variable magnetic field Hall measurement can be used to determine contributions from bulk and 2D conduction separately.

REFERENCES

[1] M. Kasu, et al., Diam. Relat. Mater. 16, 1010 (2007).
[2] D.A.J. Moran, et al., IEEE Elect. Dev. Lett. 32(5), 599 (2011).
[3] M. Kubovic, et al., Diam. Relat. Mater. 18(5-8), 796 (2009).
[4] J.E. Butler, et al., Phys. Status Solidi RRL 11(1), 1600329 (2017).

APPENDIX to Final Report

Title of Thesis: RADIATION EFFECTS IN DIAMOND SUBSTRATES AND TRANSISTORS

Aayush Thapa
Master of Science, 2019

Thesis directed by: Professor Aris Christou
Department of Materials Science & Engineering

RADIATION EFFECTS IN DIAMOND SUBSTRATES AND TRANSISTORS

by

Aayush Thapa

Thesis submitted to the Faculty of the Graduate School of the
University of Maryland, College Park in partial fulfillment
of the requirements for the degree
of Master of Science
2019

Table of Contents

List of Figures

Chapter 1: Introduction and Statement of Research Objectives

1.1 Properties of Diamond

Diamond is one of the most versatile materials with extreme physical properties. Diamond is made entirely of carbon atoms arranged much like a face centered cubic lattice, but with 4 additional atoms in tetrahedral sites, as shown in Fig 1.1 [3]. Each carbon atom forms covalent bonds with four adjacent carbon atoms, leaving behind no free electrons. This rigid structure is what gives diamond its mechanical robustness. Table 1.1 lists some of the important properties of diamond [4].

Table 1.1: Important Properties of Diamond

Property	Value	Units
Hardness	1.0×10^4	kg/mm^2
Strength, tensile	> 1.2	GPa
Strength, compressive	> 110	GPa
Young's modulus	1.22	GPa
Thermal expansion coefficient	1.1×10^{-6}	K^{-1}
Thermal conductivity	20.0	$W/cm-K$
Thermal shock parameter	3.0×10^8	W/m
Optical index of refraction (at 591 nm)	2.41	Dimensionless
Optical transmissivity (from nm to far IR)	225	Dimensionless
Loss tangent at 40 Hz	6.0×10^{-4}	Dimensionless
Bandgap	5.47	eV

Diamond's mechanical robustness and optical properties are well known. Since

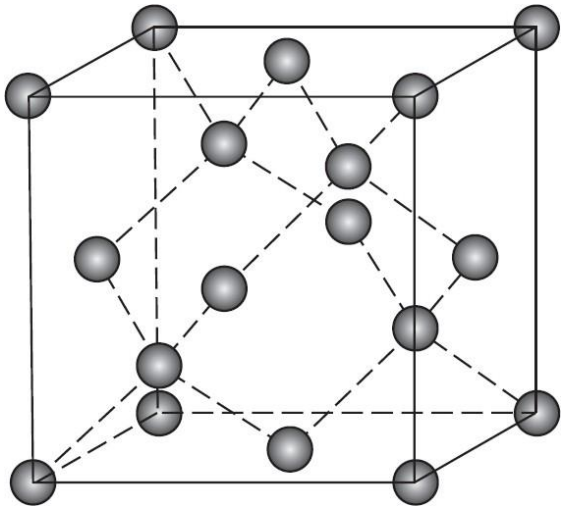

Figure 1.1: Unit cell for diamond [From [3]]

diamond is the hardest material, it has been used for a variety of mechanical applications. Furthermore, because of diamond's ultra-wide bandgap of 5.47 eV, it can transmit light across the ultraviolet to microwave range. Diamond's high hardness, high transmissivity, high thermal conductivity, and low coefficient of thermal expansion (see table 1.1) make it ideal for use for transmission windows and domes that can withstand severe environmental conditions [5] [6]. Even though diamond has been widely used for its mechanical, and, to some extent, optical properties, its excellent electrical properties have not found wide commercial application. This is mainly due to non-uniformity in naturally occuring and synthetic diamond, which has impeded the research into using diamond as an electronic-grade semiconductor material.

Recent advances in diamond synthesis by chemical vapor deposition (CVD) and high-pressure, high-temperature (HPHT) processes have led to massive reduc-

tion in nonuniformity in synthetic diamond films [7] [4]. This has been key in pushing the efforts for diamond as an electronic material.

1.2 Diamond as an ultra-wide bandgap semiconductor

Ultra-wide bandgap (UWBG) materials are materials whose bandgaps exceed those of galium nitride which has a bandgap of 3.4 electronVolts (eV). Some of the UWBG materials are beta phase of galium oxide (Ga_2O_3), aluminum nitride (AlN), aluminum galium nitride (AlGaN), cubic BN and diamond. These materials offer exciting and challenging area of research in semiconductor electronics, especially in the field of high power and RF electronics such as for high bandwidth communications, radar and intelligence applications. This is because many important parameters for device performance have highly non-linear dependence with the materials' bandgap [8]. Thus, UWBG materials have the potential to make possible devices with higher levels of performance than devices based on silicon, galium arsenide, silicon carbide or galium nitride prevelant today.

Fig 1.2 helps illustrate the non-linear scaling of device parameters such as breakdown voltage (V_{BR}) and specific on-resistance (R_{ON-SP}) with bandgap. In the figure, contours of Baliga figure of merit defined as V_{BR}^2/R_{ON-SP} for low-frequency unipolar vertical power switches is shown in log-log scale. High breakdown voltage and low specific on resistance are desirable properties. So, the higher the BFOM, the better the device properties i.e. high breakdown voltage and low specific on resistance. V_{BR} and R_{ON-SP} depend on parameters that depend on critical electric

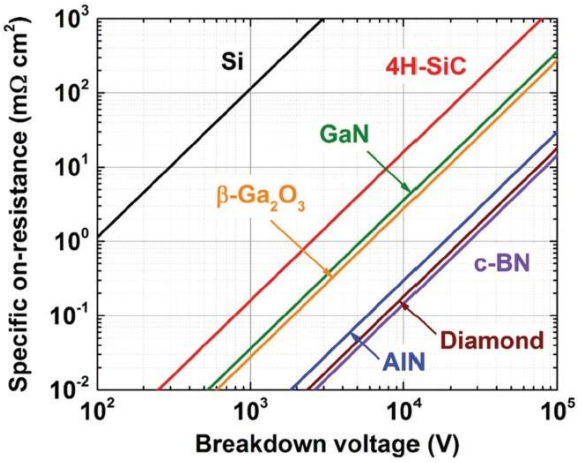

Figure 1.2: Baliga figure of merit contours for various semicondcutors for low-frequency unipolar vertical power switches [From [8]]

field (E_C) at which avalanche breakdown occurs [8] [9]. When expressed in terms of the critical electric field, the BFOM is directly proportional to E_C^3 . The critical electric field scales by about square of the bandgap. Hence, the BFOM scales as the sixth power, which explains why UWBG materials are on the lower right hand corner of fig 1.2 even on a log-log scale. It should be noted that even among the UWBG materials, diamond has one of the best BFOM.

For high-frequency, high-power applications, the Johnson figure of merit (JFOM), given by equation 1.1, is a better index for assessing the suitability of materials [8].

$$JFOM = \frac{\upsilon_{sat} E_C}{2\pi} \tag{1.1}$$

υ_{sat} is saturated carrier velocity, and E_C is the critical electric field at which avalanche breakdown occurs. υ_{sat}, E_C, and JFOM of some semiconductors are given in table 1.2 [8]. UWBG materials have higher JFOM than Si and GaN, making them suitable for high-frequency, high-power applications. Again, diamond has one of the

highest JFOM even among UWBG materials.

Table 1.2: Johnson figure of merit for semiconductor materials

Material	v_{sat} (10^7 cm s^{-1})	E_C at N_D = $10^{16} cm^{-3}$ (MV cm^{-1})	JFOM ($10^{12} V$ s^{-1})	JFOM normalized to Si =1
Si	1.0	0.3	0.48	1
GaN	1.4	4.9	11.0	23
AlN	1.3	15.4	31.9	67
$\beta - Ga_2O_3$	1.1	10.3	18.0	38
c-BN	unknown	17.3	-	-
Diamond	2.3 (e-) 1.4 (h+)	13.0	47.6 (e^-) 29.0 (h+)	100 61

Another important property for substrates utilized to make high-frequency, high-power devices is their ability to remove heat. Diamond has the highest known thermal conductivity of any material, which is what further separates it from other UWBGs with similarly high JFOM as seen in table 1.2. High thermal conductivity is of particular importance because in many power electronics and optoelectronics applications, device operation is limited by its capability to remove heat. Devices based on wide bandgap such as GaN have already encountered problems with excessive heating at high power levels, so much so that diamond layers have successfully been integrated for heatsinking [10]. Likewise, when compared to control AlGaN/GaN HEMT, nanocrystalline diamond-capped AlGaN/GaN HEMTs reduced device temperature by about 20% from 0.5 to 9 W/mm dc power device operation [11]. Diamond as heatsink layer will probably also be needed for AlGaN, AlN, and Ga_2O_3 based devices [8] [11] [12]. This necessitates research in diamond

as a semiconducting material and diamond-based devices.

Furthermore, other electrical properties of diamond such as demonstrated n-type and p-type dopability, electron and hole mobility, and critical electric field are comparable or better than other UWBG materials. Critical electrical properties of common WBG and UWBG semiconductor materials are listed in table 1.3.

Table 1.3: Electrical properties of wide- and ultra-wide bandgap semiconductors [8] [13]

	WBG		UWBG		
Material	GaN	4H-SiC	AlGaN/ AlN	$\beta - Ga_2O_3$	Diamond
Bandgap (eV)	3.4	3.3	Up to 6.0	4.9	5.5
Thermal Conductivity ($W\ m^{-1}\ K^{-1}$)	253	370	253-319	11-27	2290-3450
State-of-the-art substrate quality (dislocations per cm^2)	$\approx 10^4$	$\approx 10^2$	$\approx 10^4$	$\approx 10^4$	$\approx 10^5$
State-of-the-art substrate diameter (inches)	8 (on Si)	8	2	4	1
Demonstrated p-type dopability	Good	Good	Poor	No	Good
Demonstrated n-type dopability	Good	Good	Moderate	Good	Moderate
Electron mobility (cm^2/Vs)	2000	900		300	4500
Hole mobility ($cm^2/V\ s$)	200	120			3800
Breakdown field (MV/cm)	3.3	2		8	10

1.3 Doped Diamond Substrates

Field effect transistors (FETs) based on diamond rely on conductive channel formed by unconventional means. This is because substitutional doping in diamond results in deep donor and acceptor states. The deep acceptor states (0.37 eV for boron) and deep donor states (0.7 eV for nitrogen, and 1.3 eV for phosphorous) cause low activation at room temperature [16]. There is heavy interest in two current solutions: surface terminating with hydrogen, and incorporating a thin heavily boron doped layer buried few tens of nanometers from the surface. Both of these methods result in the formation of a 2D conduction channel.

Hydrogen termination of diamond leads to a negative electron affinity (NEA) of its surface. This NEA surface loses electrons to adsorbed gaseous species such as atmospheric moisture, NO_2, or high electron affinity oxides [14]. These physically adsorbed species act as surface transfer dopants, generating a conductive two-dimensional hole gas (2DHG) near the surface [15].

During epitaxial growth, extremely high concentration of boron i.e. greater than 10^{20} cm^{-3} is incorporated, which creates a confined hole channel layer. This thin layer of about 1-3 nm buried a few tens of nanometers from the top surface is what is termed the delta layer. Based on 2D densities of holes, fraction of holes located outside of heavily doped region, in the lightly doped and high mobility region was calculated and where the 2DHG channel is predicted to form.

FETs have been fabricated successfully based on p-channel formation in diamond in the ways mentioned above. To date, the highest reported maximum drain

current density for diamond devices is -1.35 A/mm for H-terminated substrates [17]. Likewise, Kawarada et al. have demonstrated stable operation of diamond devices based on H-terminated substrates at temperatures up to 400°C in vacuum [18].

1.4 Radiation Effects

Diamond is predicted to be radiation hard i.e. resistant to radiation damage. This is because of its ultra-wide bandgap and high binding energy of its covalent carbon to carbon bonds. A measure for accessing potential radiation hardness of materials is the threshold displacement energy, which is the minimum kinetic energy required by an atom in a solid to be parmanently displaced from its lattice site. Diamond has a displacement energy of 43 eV, whereas other semiconductors such as Si has 13-20 eV, 4H-SiC has 21.8 eV, and GaAs, 10 eV [20]. Thus, in addition to mechanical robustness, and promising electrical properties, diamond potentially also has high radiation tolerance. So, diamond-based electctronics could be used in extremely harsh environments subject to high temperature, pressure and/or radiation. These electronics could be subjected to protons, alpha particles and electrons in the low earth orbit satellites, and to neutrons or gamma rays in nuclear reactors and military systems [22]. While many radiation damage studies have been conducted with regards to diamond as detectors, not many have been done investigating radiation effects in diamond transistors [19]. Radiation damage studies in diamond from device point of view is especially important because diamond devices are based on unconventional p-channel formed by surface hydrogen termination or

by heavily boron doped delta layer, which may be succeptible to radiation damage.

The only prominent study on radiation effects on diamond devices was done by Verona et al. who conducted neutron irradiation experiments on H-terminated diamond substrates and devices [19]. Diamond was found to have stable device performance after irradiation with 14.8-MeV neutrons. The effects of other types of radiation on H-terminated or delta-doped substrates and devices are unknown. This thesis addresses part of this issue by investigating the effects of both ionizing radiation in the form of protons, as well as that of non- ioninizing radiation in the form of gamma rays on diamond substrates and devices. These two different types of radiation was selected because the interaction of semi- conductors with a neutral radiation like gamma rays is fundamentally different than that with a charged particle like proton [22]. The energy loss mechanisms for protons are Rutherford scattering, knock-on atoms, and energy loss to ionization, whereas that for gamma rays are the photoelectric effect, Compton scattering, and pair production [23].

Rutherford scattering causes lattice damage by displacing atoms from its lattice site. This occurs when an atom in a solid scatters a charged particle like protons and the reaction on it is strong enough to displace it from its lattice site. Furthermore, if the displaced atom has sufficient energy, it may displace additional atoms, called knock-on atoms, creating more defects. This effect is prevelant for heavy particles such as protons. Also, charged particles passing through a material will ionize it if the velocity of the charged particles is greater than that of the electrons in the material. Likewise, gamma radiation may cause ionization effects as well as

displacement of atoms. Compton scattering is the dominant lattice damage mechanism for gamma rays below 15 MeV. It occurs when a gamma ray photon interacts with a valence band electron and transfers portion of its energy to the electron, causing the gamma photon to be scattered and the electron to be ejected from the atom. This recoil electron is what damages the lattice. Detailed information on the interactions and effects of different types of radiation on different WGB and UWBG semiconductor materials and devices can be found in [19] - [25].

Chapter 2: Materials and Methods

2.1 Diamond Substrates

New Diamond Technology supplied undoped (100) type IIa single crystal high pressure high temperature (HPHT) substrates to the University of Maryland. This type of substrates was selected because of their very low dislocation density, as dislocations could act as carrier scattering centers. These substrates ranged between 3 mm × 3 mm to 4.5 mm × 4.5 mm in length and width, and 0.5 mm in thickness. These substrates were polished and etched with a low power plasma to reduce the possibility of scattering further.

Both H-terminated and delta-doped diamond substrates were used in this thesis. Hydrogen-plasma treatment was performed to achieve hydrogen termination on these substrates, whereas delta-doped samples were obtained by incorporating a heavily doped boron layer during epitaxial growth using Chemical Vapor Deposition (CVD).

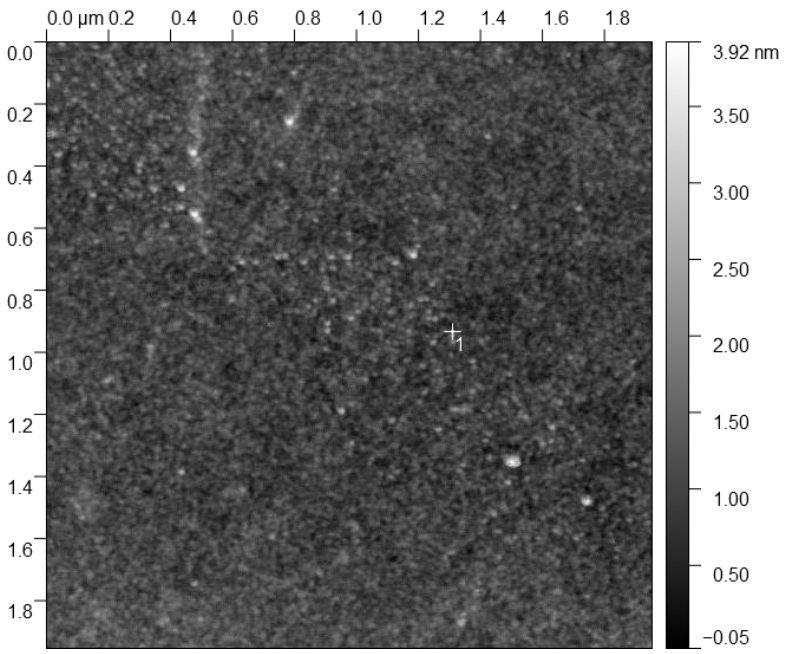

Figure 2.1: AFM image of a polished diamond surface with less than 0.3 nm RMS roughness

2.1.1 H-terminated Diamond

For H-terminated diamond samples, RMS roughness value of less than 3 Å was determined using atomic force microscopy (AFM), wihch verified the effects of polishing and etching. An AFM micrograph of a sample shown in Fig. 2.1 whose RMS surface roughness was found to be less than 0.3 nm.

The substrate surface was exposed to a hydrogen plasma at temperatures above 700°C to achieve hydrogen termination. To confirm whether hydrogen termination was achieved, Fourier transform infrared spectroscopy (FTIR) was used. The FTIR spectrum shown in Fig. 2.2 has peaks between 2800 and 3000 cm^{-1}, which correspond to C-H bonds [26].

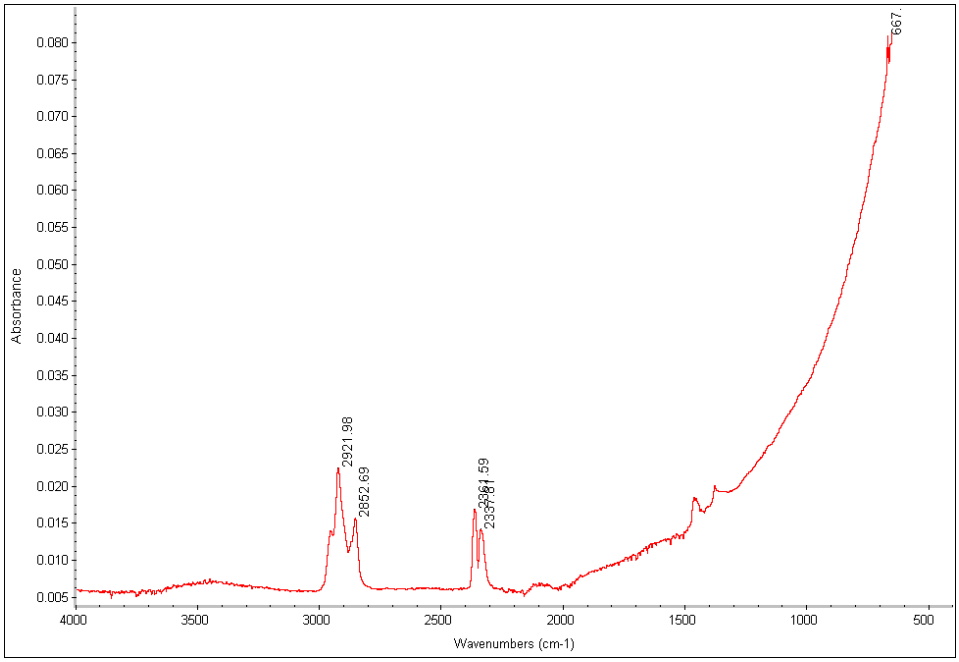

Figure 2.2: FTIR Spectrum of H-terminated Diamond Sample showing peaks between 2800 and 3000 cm^{-1} corresponding to C-H bonds

Likewise, the effect of H-termination i.e. the formation of conductive layer was observed by performing a simple current-voltage measurement between two gold contact pads on the hydrogenated sample. Fig. 2.3 shows that H-terminated surface had linear current-voltage response, whereas when the H-termination was replaced with oxygen, there was barely any voltage response to applied current compared to that of the H-terminated diamond.

2.1.2 Delta-doped Diamond

As opposed to H-terminated diamond, delta doped diamonds had epitaxial layer grown on the HPHT substrate with 1-3 nm of heavily doped-boron delta layer incorporated in the epi-layer. Fig 2.4 shows AFM image of delta-doped diamond

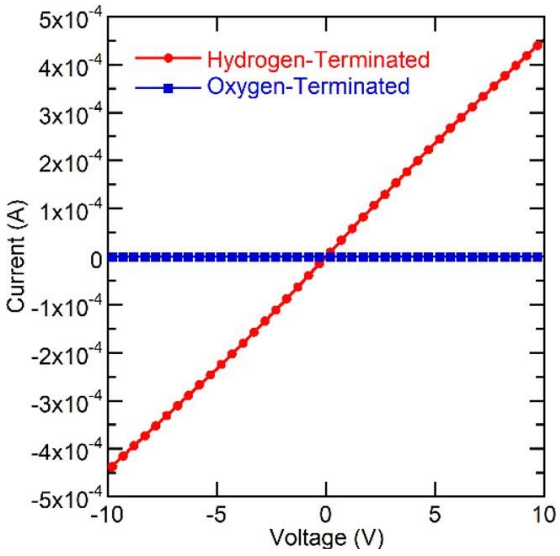

Figure 2.3: Current-Voltage (I-V) characteristics for H-terminated versus O-terminated diamond substrate [From [2]]

whose surface roughness is less than 0.3 nm.

Two different types of delta-doped diamonds were used: single delta-doped and double delta-doped. Single delta-doped diamond had only one 2-nm delta layer buried 12 nm from the surface, whereas double delta-doped diamond had two heavily B-doped delta layers. The first delta layer was at 26 nm from the top surface, and the second delta layer was right at the surface. The SIMS profile in fig 2.5 shows the two layers for the double delta doped sample.

2.2 H-terminated Devices

Surface transfer dopants such as H_2O, NO_2 and NO are unstable, and thus, problematic in fabricating relaiable devices. High electron affinity dielectrics are better suited as surface transfer dopants for H-terminated devices. In this work,

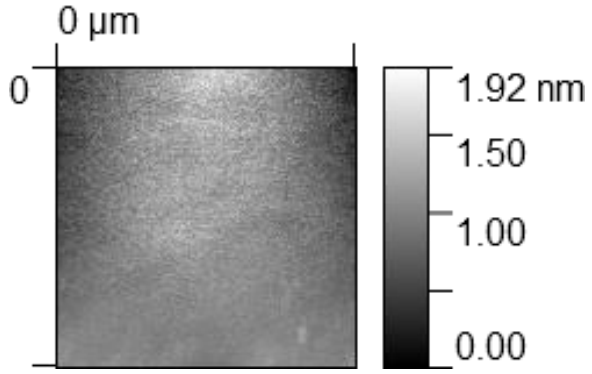

Figure 2.4: AFM image ($1\mu m \times 1\mu m$) of a polished delta-doped diamond surface with less than 0.3 nm RMS roughness

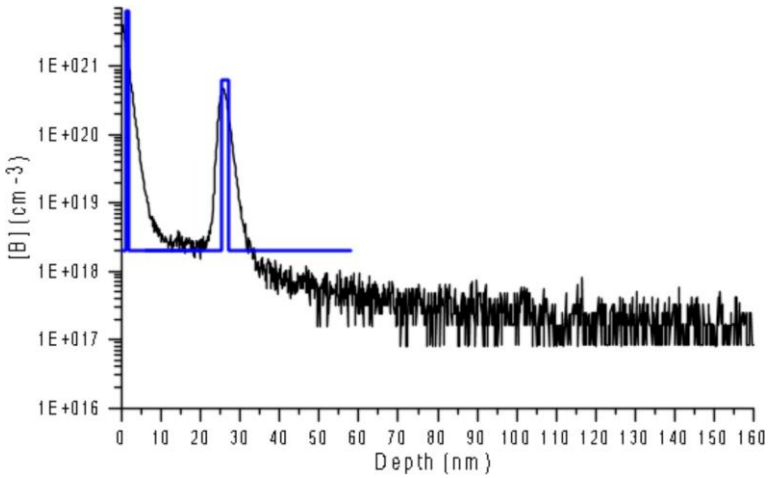

Figure 2.5: SIMS profile for double delta-doped diamond sample

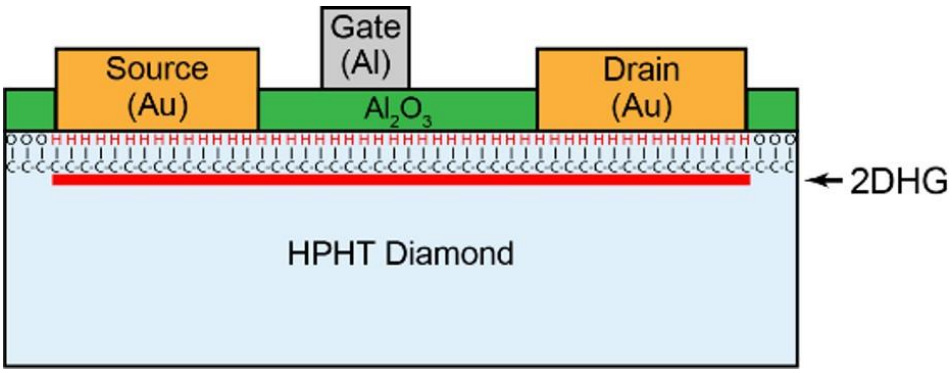

Figure 2.6: A schematic of H-terminated diamond based MOSFET device with Al_2O_3 as surface transfer dopant which leads to the 2DHG channel [From [2]]

aluminum oxide, Al_2O_3, was used as gate oxide.

A schematic of MOSFETs fabricated using HPHT hydrogen terminated substrates is shown in Fig. 2.6. A blanket Au layer of 100-150 nm was evaporated on the surface of the hydrogen terminated substrate. This ensured protection of the surface hydrogen termination responsible for the conducting channel under each device. Device mesas were created by patterning photoresist on top of the blanket Au layer and using etchback process with KI/I_2 wet etchant. To isolate the devices, O_2 plasma etch was employed which replaced C-H bonds with C-O bonds between devices, effectively eliminating 2DHG channel underneath. Again, photoresist was patterened and KI/I_2 wet etchback was performed to form discrete Ohmic contacts from the Au mesas. 25 nm of Al_2O_3 was deposited by atomic layer deposition (ALD) at 175°C. Then, using e-beam and liftoff processes, 100 nm of Al gate was deposited.

2.3 Temperature Dependent Hall Effect Measurement

2.3.1 Background

The Hall effect is a technique used to distinguish carrier type of a semiconductor, to measure majority carrier mobility and majority carrier concentration. It is based on the Lorrentz force given by equation 2.1 exerted on moving charges.

$$F = qv \times B \tag{2.1}$$

When current is passed in one direction along the surface of the semiconductor and the magnetic field is perpendicular to the surface of the semiconductor, the force experienced by moving charges will force the charges to accumulate in perpendicular direction to the direction of motion of the original current. This buildup induces an electric field in the opposite direction, balancing the magnetic field force. This induced electric field is callled the Hall field, which is responsible for producing the Hall voltage – a voltage difference across the semiconductor surface, perpendicular to the direction of injected current. The polarity of Hall voltage is evidence of the carrier type. Furthermore, the Hall voltage along with the applied current, magnetic field, and sample dimensions help determine the majority carrier concentration and the majority carrier mobility.

2.3.2 Van der Pauw Technique

The Hall effect can be measured using different configurations. This methodology presented here is based on the work of Van der Pauw with guidelines from

ASTM standard F76-08 [28].

Van der Pauw technique helps determine an arbitrarily shaped sample's resistivity and, in presence of a magnetic field, the hall coefficient. For this, four ohmic contacts must be made at the surface, as close to the edges (corners, for square samples) as possible. Together, the resistivity and the hall cofficient are used to obtain hall mobility.

2.3.2.1 Resistivity Determination

Resistivity is determined by measuring voltage response across adjacent contacts by passing current through the other pair of contacts. Measurement accuracy is improved by repeating the process to get voltage response from each adjacent pair of hall pads which amounts to 4 total measurements. Furthermore, the polarity of the current source and voltage for each of these 4 measurements is switched to give 4 additional data points. Thus obtained data points are used in equations 2.2 and 2.3 to calculate resistivity values, the average of which is taken as the resistivity of the sample.

$$\rho_A = \frac{\pi}{4ln(2)} \frac{f_A t}{1} (V_{21,34} - V_{12,34} + V_{32,41} - V_{23,41}) \tag{2.2}$$

$$\rho_B = \frac{\pi}{4ln(2)} \frac{f_B t}{1} (V_{43,12} - V_{34,12} + V_{14,23} - V_{41,23}) \tag{2.3}$$

f_A and f_B are geometrical factors based on sample symmetry. In case of perfect symmetry, $f_A = f_B = 1$. The geometrical factors f_A and f_B are determined by

corresponding resistance ratios given by equations 2.4 and 2.5 respectively.

$$Q_A = \frac{V_{21,34} - V_{12,34}}{V_{32,41} - V_{23,41}} \tag{2.4}$$

$$Q_B = \frac{V_{43,12} - V_{34,12}}{V_{14,23} - V_{41,23}} \tag{2.5}$$

Equation 2.6 is then used to find the appropriate geometrical factors, f_A and f_B, which are used in equations 2.2 and 2.3 respectively to get resistivity values. If Q obtained from equation 2.4 or 2.5 is less than 1, then its reciprocal must be used to find f.

$$\frac{Q-1}{Q+1} = \frac{f}{0.693} arccosh f_{1/2} \, exp \, \frac{0.693}{f} \tag{2.6}$$

Finally, the average resistivity, ρ_{avg}, is calculated as follows:

$$\rho_{avg} = \frac{\rho_A + \rho_B}{2} \tag{2.7}$$

2.3.2.2 Hall Cofficient Determination

To determine Hall Coefficient, magnetic field is applied such that the magnetic flux is perpendicular to the sample's surface. Current must be passed diagonally through the sample, say leads 1 and 3, and voltage difference measured at the pads on the other diagonal, in this case, leads 2 and 4. Additional measurements under reverse current is also obtained. Furthermore, the polarity of magnetic field is switched, and voltage measurements for both forward current and reverse current are taken. These voltage measurements in V along with magnetic flux in $Gauss$, current in A, and thickness of the sample in cm are used in equations 2.8 and 2.9 to get two hall coefficients in cm^3C^{-1} for the two diagonals of

$R_{HC}R_{HD}$

The Hall-coefficient is then calculated as follows:

$$R_{Havg} = \frac{R_{HC} + R_{HD}}{2} \tag{2.10}$$

$$= 2.50 \times 10^{7} \frac{t}{BI} [V_{31,42(+B)} - V_{13,42(+B)} + V_{13,42(-B)} - V_{31,42(-B)}] \tag{2.8}$$

$$= 2.50 \times 10^{7} \frac{t}{Bl} [V_{42,13(+B)} - V_{24,13(+B)} + V_{24,13(-B)} - V_{42,13(-B)}] \tag{2.9}$$

2.3.2.3 Hall mobility and carrier concentration

Resistivity and hall coefficient values thus evaluated are used to determine hall mobility in $cm\ V^{-1}s^{-1}$ using the equation for average Hall mobility from first determining the Hall coefficient.

$$\underline{R_{Havg}} \tag{2.11}$$

The drift mobility, μ, in a single carrier sample is related to the average Hall mobility by a proportionality constant:

$$\mu_{Havg} = r\mu \tag{2.12}$$

Equation 2.13 shows relation between the Hall coefficient and carrier concentration for extrinsic semiconductors, given that the measurement temperature is below the intrinsic region with conduction dominated by a single carrier type.

$$R_{Havg} = \frac{r}{nq} \tag{2.13}$$

Where r is proportionility constant on the order of unity, q is elementary charge, and n is carrier concentration.

2.3.3 Activation Energy Determination

Temperature dependence of conductivity of a material, which is the reciprocal of resistivity, can be used to extract its activation energy. Fig. 2.7 shows conductivity curve for most semiconductors [29]. At lower temperatures, conduction

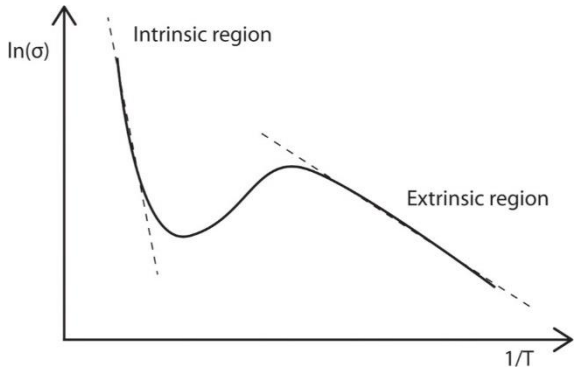

Figure 2.7: Expected behavior of natural log of conductivity versus reciprocal temperature for a doped semiconductor (Taken from [29])

extrinsic carriers dominates, as there is not enough energy for activation of intrinsic carriers. At high enough temperatures when activation energy becomes equal to or greater than the intrinsic bandgap, conduction through intrinsic carriers dominates. Conductivity of a semiconductor is given by:

$$\sigma = (n\mu_e + p\mu_h)e \tag{2.14}$$

The electron and hole carrier concentrations are functions of density of states in the conduction and valence bands for intrinsic conduction, and that of density of states in donor or acceptor states for extrinsic conduction. Carrier concentrations which are equal for intrinsic semiconductor are given by equation 2.15 in which 'C' is a constant.

$$n = p = CT^{\frac{3}{2}} e^{-\frac{Eg}{2kT}} \tag{2.15}$$

From equations 2.14 and 2.15, the following relationship is obtained for conductivity. Since 'T' in exponential term overshadows $T^{\frac{3}{2}}$, this term can be ignored. Taking natural log of both sides yields activation energy in the form of E_g from the slope

of lnσ versus 1/T relationship, as described by 2.18 which is seen in Fig 2.7.

$$ln\sigma = ln[C(\mu_e + \mu_h)e] + lnexp(-Eg/2kT) \quad (2.17)$$

$$ln\sigma = \left(\frac{-E_g}{2k}\right)\frac{1}{T} + ln[C(\mu_e + \mu_h)e] \quad (2.18)$$

2.3.4 Sample Preparation

The HMS-5000 System at the University of Maryland's Nanocenter was used to measure the temperature dependent Hall parameters. This system has four gold probes which measure current-voltage characteristics. Van Der Pauw configuration was patterned on the samples, and the samples were mounted on HMS-5000 System for Hall measurements. The details of this process are given below.

2.3.4.1 Contact Metal Deposition

First, the samples were cleaned by sonicating them in acetone for 30 minutes and blow-drying with nitrogen gun. To deposit contact metal only on the corners, silicon piece was used as a mask. The silicon mask was attached to the sample using double sided kapton tape. This Si piece covered the entire surface of the sample, exposing only the corners. Contact metal was then evaporated using the Angstrom e-beam evaporator at the Maryland Nanocenter. 25 nm layer of chromium was first diposited as adhesion layer, followed by 250 nm layer of gold without the interruption of vacuum, which was around 4×10^{-6} torr. Fig. 2.8 shows a sample with the contacts thus deposited.

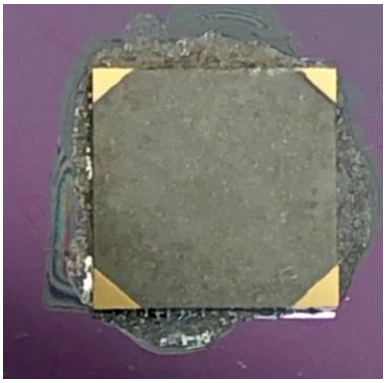

Figure 2.8: Cr/Au contacts on the corner of the diamond sample for Hall Effect Measurement using the Van Der Pauw Technique

2.3.4.2 Sample Mounting

All of the diamond samples were less than 3.5 mm × 3.5 mm in size. This posed a problem, as the HMS-5000 System used for Hall measurements could not accomodate substrates smaller than 5 mm × 5 mm. HMS-5000 System's probes could not be moved to be placed on the corners of the samples where contact pads were deposited. Thus, a work-around was established in order to be able to use the HMS-5000 System. Diamond sample was placed on top of silicon dioxide (SiO_2), which is a great electrical insulator. Bondwires were drawn from the contact pads on diamond corners to contact pads on silicon dioxide substrate. This effectively extended the contact pads of diamond samples so that the probes of the HMS-5000 System could reach the small diamond samples and measure their properties. The sample set up along with the four probes of the HMS System is shown in Fig. 2.9.

The SiO_2 substrates were obtained by thermally growing 1 micron layer of SiO_2 on a Siicon wafer. Then, 40 nm layer of chromium was evaporated on the

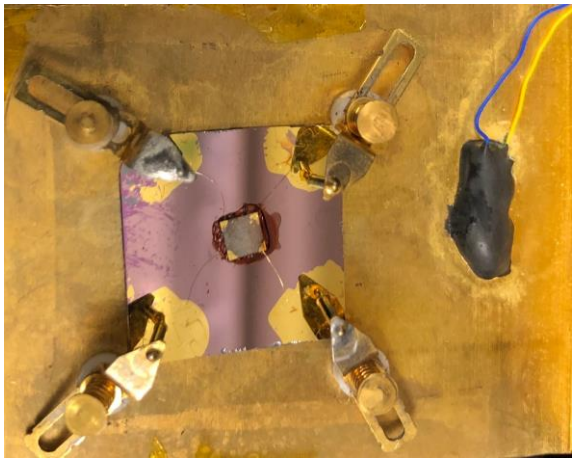

Figure 2.9: Diamond sample on top of the non-conductive Silicon dioxide for Hall measurements using HMS-5000 System. Wirebonds are drawn from the contact pads on diamond to contact pads on SiO_2 on which probes of HMS-5000 System are dropped

entire wafer, followed by 400 nm of gold in the Angstrom e-beam evaporator under high vacuum (i.e. $< 5 \times 10^{-6}$ torr) without interruption. The 3-inch wafer was cleaved into several smaller pieces which fit the sample size specification of the HMS-5000 system. These smaller pieces were prepared such that each had four distinct regions with metal on top. To do this, photoresist was deposited on the corners to shield those areas. Metal was etched from the remaining bulk of the area by a 2-step wet etching process. First, gold was stripped off using KI/I_2 solution (Au Etchant TFA, Transene Co.). Once gold had come off, the pieces were immersed in ceric ammonium nitrate and nitric acid (Chromium Etchant 1020, Transene Co.) for Cr etching until the SiO_2 surface was exposed. Finally, the sample was cleaned in acetone and isopropyl alcohol (IPA) to remove the resist from the corners.

LOR7B resist was used to attach a diamond sample each to the bare SiO_2

part of each of the mount pieces by hardbaking it at 180°C for 45 minutes. Then, a semi-automatic wire bonder (West Bond 454647E) was used to connect bondpads on diamond and SiO_2 through bondwires. The SiO_2 substrate with the diamond thus mounted was placed in the stage of the wirebonder, which was heated at 100°C. The stage was heated because bondwires stick to bond pads relatively easily when the bond pads are at high temperature. LOR7B was selected as an adhesive precisely for this, as it provided sturdy adhesion even at such temperatures whereas other available photoresists such as MicroChem's 1813 and 1805 would start to liquefy. This is because the LOR's softening temperature was higher than the stage's temperature, whereas that of 1813 and 1805 resists were lower. Double sided Kapton tape would have been easier to work with, however, its adhesion was not sturdy enough, and the sample would move. This meant that the bondwires would not stick on the diamond's contact pads. Once wirebonding was complete, the samples were ready for Hall measurements.

The probes of the HMS-5000 system were dropped on the metal regions of SiO_2 to probe the diamond sample. Since diamond has lower bandgap than SiO_2, the easiest conduction path is through the metal wire and across the diamond. To ensure that SiO_2 substrates were not affecting the results, HMS-5000 System was run for SiO_2 substrates without diamond on top. The software gave no voltage readings for the entire input current range, and would read "Contact fail." This is because resistivity of SiO_2 is higher than the upper limit for resistivity of HMS-5000 System. Thus, when diamond was mounted on SiO_2 substrate, the voltages were now being measured across the contact pads in the diamond because diamond's

resistivity (much lower than that of SiO_2) was within the limits of this instrument.

2.4 Radiation

Radiation hardness of diamond is an appealing prospect for diamond-based sensors and devices. This works explores diamond's radiation hardness against gamma rays in H-terminated devices for change in output characteristics. This work also delves into the effects of proton irradiation on transport characteristics through Hall effect measurements.

Firstly, radiation stability of H-terminated diamond field effect transistors were explored. These FETs were subjected to gamma irradiation at the University of Maryland Radiation Facilities (UMRF). High capacity dry cell, panoramic gamma irradiator was used with ^{60}Co as source material for gamma irradiation. ^{60}Co source decays to release 1.17 and 1.33 MeV gamma rays. The devices were subjected to irradiations from a total dose of 1 kRad(Si) up to 26 MRad(Si), depending on the devices available and schedule of radiation facility.

Additionally, radiation hardness of the bare H-terminated and delta-doped substrates was investigated. For this, UMRF's cyclotron was used to irradiate the sample substrates with protons. Fig 2.10 shows the cyclotron chamber. The tube-like structure on the bottom right extending from outside the chamber to near the center is the linear positioner for sample stage. The spot size of the proton beam was just enough to accomodate the entire surface area of the 3.5 mm × 3.5 mm sample on the stage. Thus, the samples had to be carefully placed, and parameters

optimized in order to get uniform coverage of the entire surface with protons. The cyclotron frequency was set to 7.15 MHz, and magnetic field was 0.47 T. The sample was placed 12 cm from the center of the cyclotron chamber. From these parameters and the kinetic energy relation, energy of the protons was calculated to be 152 keV. Beam current, spot size of the beam, and irradiation run time were used to determine the fluence of the protons. The beam current determined using Ohm's law was 73.6 nA for a voltage drop of 73.6 mV with a resistance of 1 MΩ. To help estimate the spot size of the beam, phosphor background was used in the sample holder. This is because phosphor glows brightly whereever the beam strikes it, making it easy to determine the spot size. Fig. 2.11 shows the sample holder with an H-terminated sample and a delta-doped sample being irradiated. The spot size was estimated to be 269 cm^2. For 73.6 nA beam current, 269 cm^2 spot size and considering 10% duty cycle for a run time of 100 minutes, the fluence was calculated to be 1.03×10^{12} protons/cm^2.

2.5 Device Simulation

Modeling of device I-V characteristics was done in order to understand the effect of radiation on device performance. The quadratic model for constant mobility assumption was used to model DC characteristics of diamond-based FETs. Mobility values for this model was obtained from Hall measurements for pre and post-proton irradiation. Modeling is done in Matlab based on equation 2.20 for

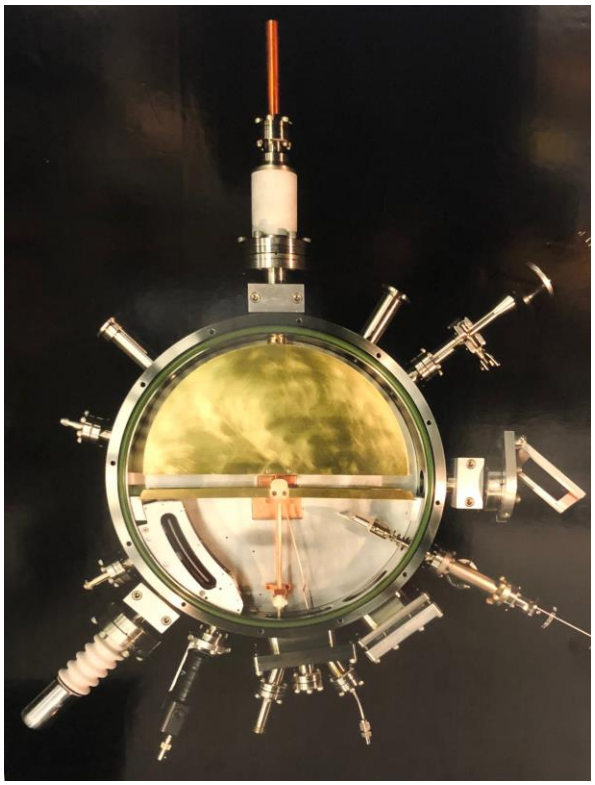

Figure 2.10: Cyclotron chamber

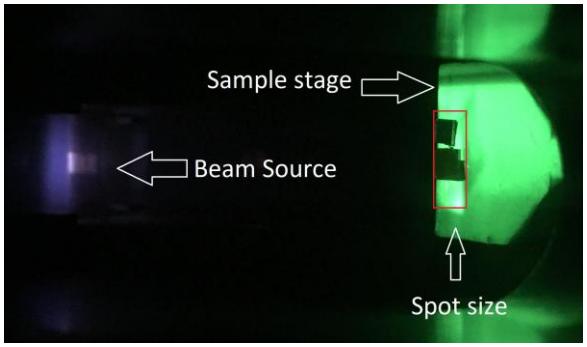

Figure 2.11: Diamond substrates being irradiated with protons in the cyclotron

p-channel depletion mode.

$$\beta = \frac{E\mu_p W_G}{d_i L_G} \tag{2.19}$$

$$I_D = \beta \ \ (V_g - V_{th}) V_{DS} - \frac{V_{DS}^2}{2} \tag{2.20}$$

Where E is dielectric constant of gate insulator, μ_p is mobility, W_G and W_L are gate width and gate length respectively, d_i is dielectric thickness, I_D is drain current output, V_g is gate voltage, V_{th} is threshold voltage, and V_{DS} is drain-source voltage.

Chapter 3: Results and Discussion

3.1 H-terminated FET Radiation Effects

H-terminated FETs were subjected to gamma radiation at low dose from 1 to 100 kRad(Si) as well as high dose up to 26.3 MRad(Si). Fig 3.1 shows device characteristics at 0 kRad i.e. pre-irradiation, 1 kRad, 2 kRad, 3 kRad, and 100 kRad dose. At an initial dose of 1 kRad, drain current, threshold voltage, and transconductance decreased, while no significant change was observed for on-resistance. These characteristics were stable after irradiation up to a dose of 100 kRad. Campbell and Mainwood reported 0.03 and 0.09 vacancies/gamma per cm in diamond by gamma irradiation of 1 and 2 MeV respectively [23]. Thus, the slight decrease in output characteristics may be because of the introduction of defects acting as scattering centers.

High dose irradiation led to the opposite effect for drain current output, as shown in 3.2. At 13.6 Mrad dose, drain current increased significantly. Upon further irradiation at a total dose of 26.3 MRad, drain current remained the same. High dose irradiation seems to have resulted in an annealing effect. The increased drain current response after irradiation could be due to the formation of defects at oxide interface. These defects form trap states, resulting in enhanced hopping conductivity

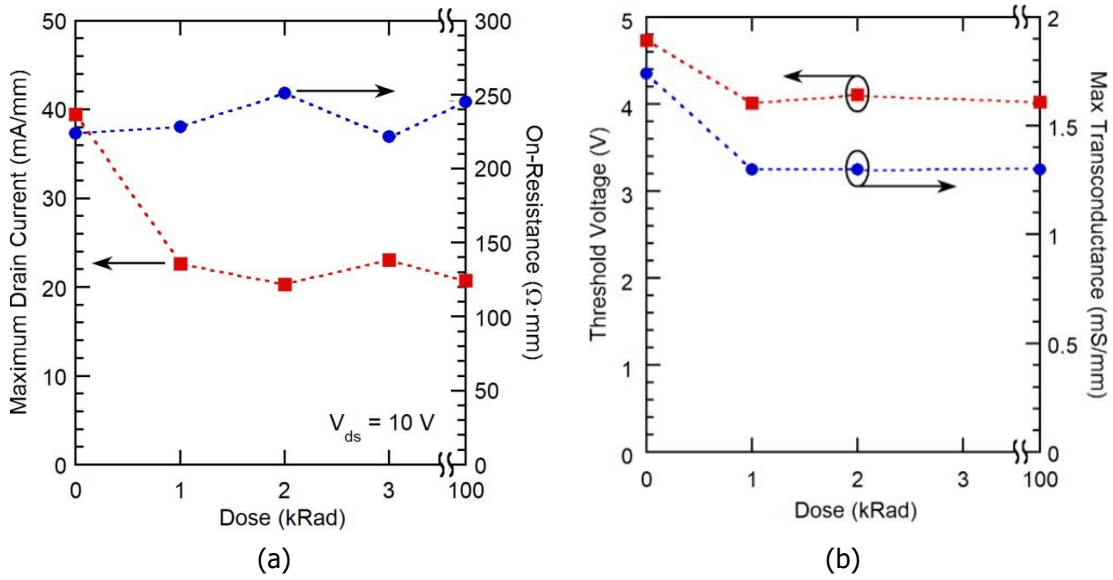

Figure 3.1: Device characteristics at low-dose (≤100 kRad) gamma irradiation [1]

which led to the increase in current output. Also, threshold voltage to turn off devices increased significantly from 5 V pre-irradiation to about 9 V post-irradiation. However, gate leakage current showed no significant increase post-irradiation.

3.2 Pre-irradiation Hall Measurement

Hall measurements were taken for H-terminated and delta doped samples before irradiating these samples. The upper limit of the temperature range for these measurements was 350 K because that is the upper limit for HMS-5000 system, and the lower limit varied based on the sample, as it depends on sample's resistivity.

3.2.1 H-terminated diamond

HMS-5000 System was used to determine whether or not the contacts exhibited ohmic behavior, in other words, linear current-voltage (I-V) relationship. Current

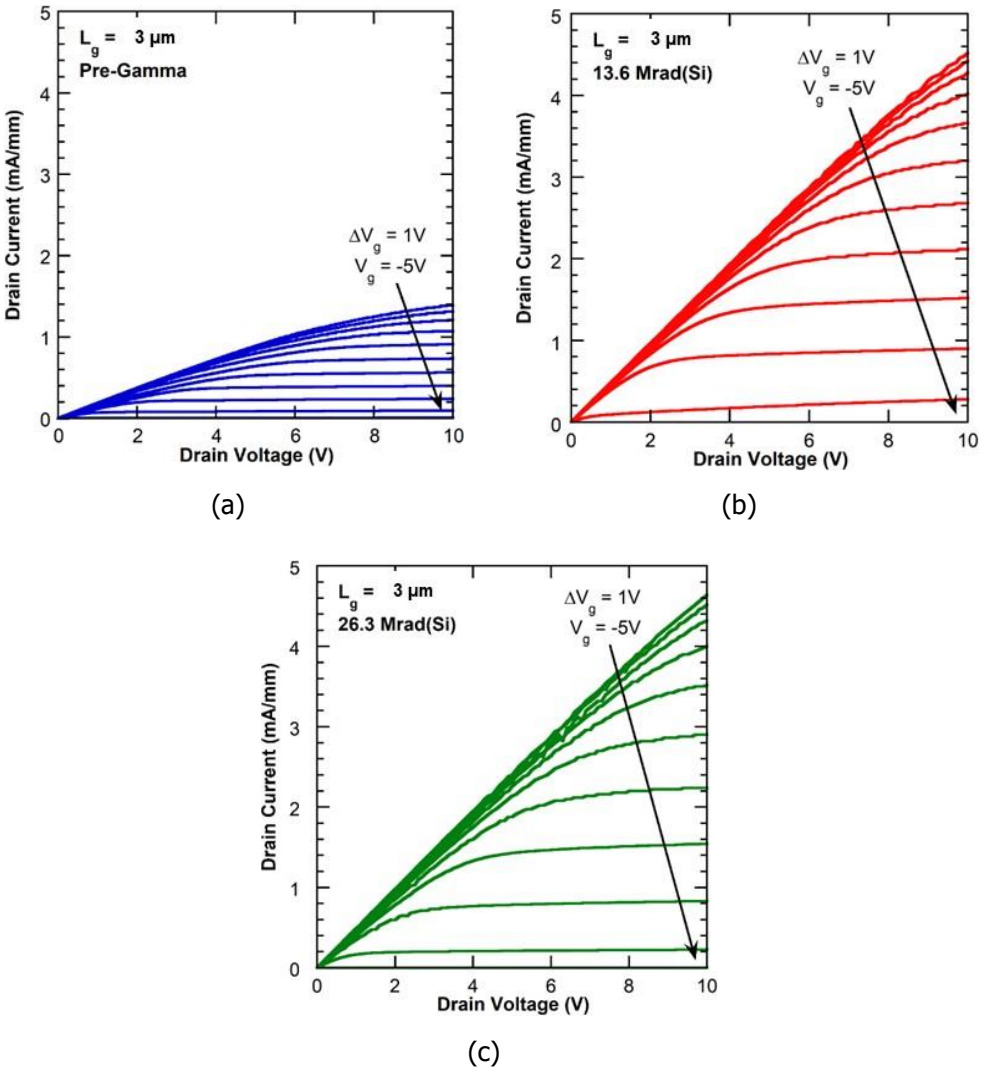

Figure 3.2: Drain current versus drain voltage for (a) pre-irradiation, (b) post-13.6 Mrad, and (c) post-26.3 MRad of gamma irradiation [1]

was passed through adjacent contact pads, and voltage difference measured.

H-terminated diamond was annealed after metal deposition at 550°C for 1 minute. Rapid thermal annealing (RTA) was performed using RTA-610 device in N_2 environment. Fig 3.3 shows I-V behavior at substrate temperature of 298 K for four adjacent contact pads ab, bc, cd, and da. The linear relationship proves ohmic behavior, however, the difference in voltage response for the four pairs of

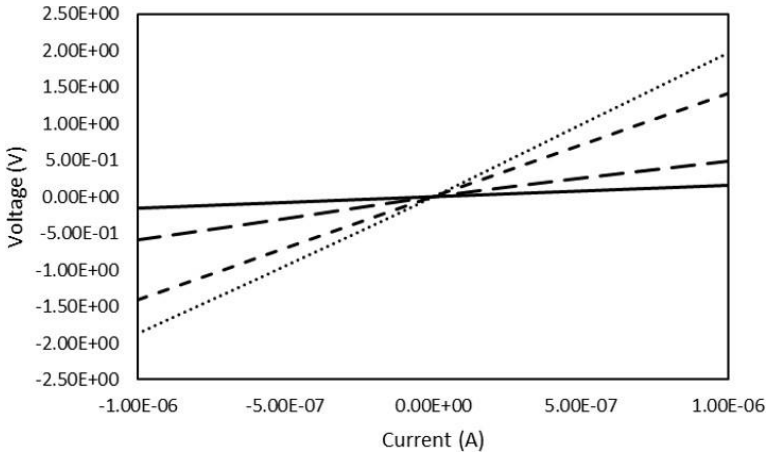

Figure 3.3: I-V curves at 298 K substrate temperature for H-terminated diamond annealed at 550°C for 1 minute in RTA

contact pads indicates non-uniformity. This could be because of non-uniform surface termination with hydrogen.

I-V curves were also obtained at substrate temperature of 250 K as shown in Fig 3.4. The voltage response of each contact pair increases by an order of magnitude compared to I-V curves at room temperature. Furthremore, two contact pad pairs plateau at current higher in magnitude than about 0.6 μA and 0.7 μA, deviating from linear ohmic behavior. Thus, when performing Hall measurements at temperatures lower than about 288 K, 0.1 μA current was used to be in the linear I-V region, whereas for temperatures higher than that, 1 μA was used for better accuracy.

Current-voltage measurements, as outlined in section 2.3.2, were performed for each temperature step in the range from 250 K to 350 K. For almost all of the data points, Hall coefficients calculated were positive as expected for semiconductor

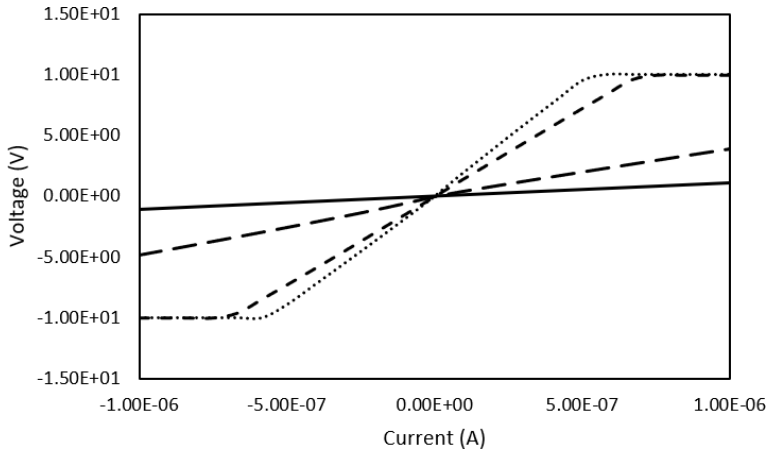

Figure 3.4: I-V curves at 250 K substrate temperature for H-terminated diamond annealed at 550°C for 1 minute in RTA

with p-type carriers. The occasional negative hall coefficients must be due to non-uniformity in ohmic contact pads and random fluctuations.

Fig 3.5 shows natural logirathm of conductivity as a function of reciprocal temperature for two sets of data points taken for temperature range of 250 K to 350 K at an increment of 1 K. HMS-5000 System datapoints are based on conductivity output from the HMS-5000 System software, and the Calculated (ASTM) datapoints are based on data analysis according to ASTM standards outlined in [28]. HMS-5000 System software calculated higher resistivity (thus, lower conductivity) than that calculated using ASTM standards for Van der Pauw configuration. This difference is about an average of 45% for all data-points. Refering back to equations 2.2 and 2.3, this difference in the two datasets for resistivity arises from the geometrical factors f_A and f_B determined for the two datasets. The method of determination of f_A and f_B by the HMS-5000 System software is unknown, whereas that for Calculated

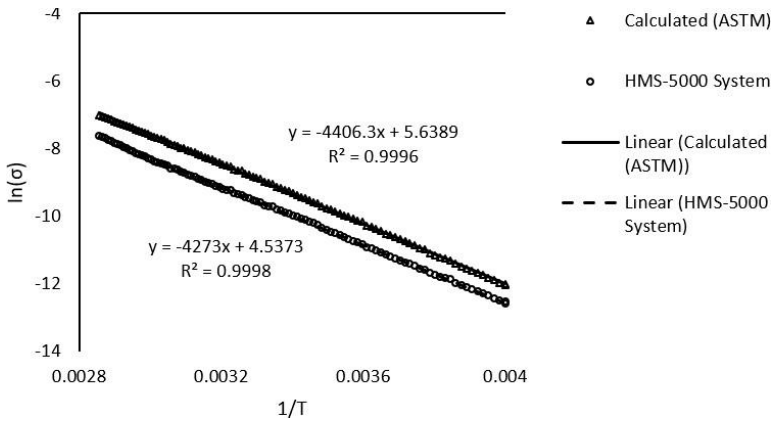

Figure 3.5: Natural logarithm of conductivity versus reciprocal temperature for H-terminated diamond for data output by HMS-5000 System software and data analyzed using ASTM standards [28], as well as the trendlines for both data sets with information about its slope

(ASTM) dataset was by using ASTM Standards by satisfying equation 2.6. Thus, there is more confidence in the accuracy of the dataset obtained by following the ASTM Standards. The slopes of -4406.3 K and -4273 K for Calculated and HMS-5000 datasets give activation energy (E_g) of 0.76 eV and 0.74 eV respectively. Since, conduction is through p-type carriers, it must be through movement of holes as this sample has no ionic charge carriers. Furthermore, the activation energy of 0.76 eV indicates that there is shallow acceptor level sitting below the Fermi energy level and 0.76 eV above the valance band.

Similarly, fig 3.6 shows temperature dependence of mobility for H-terminated diamond. At 300 K, mobility of 128.3 $cm^2 V^{-1} s^{-1}$ was obtained from calculations based on ASTM standards [28], whereas that of 64.5 $cm^2 V^{-1} s^{-1}$ was obtained from calculations based on HMS-5000 System software. This is close to the mobility value of 68 $cm^2 V^{-1} s^{-1}$ reported by Verona et. al. [14], whereas the ASTM-based value is

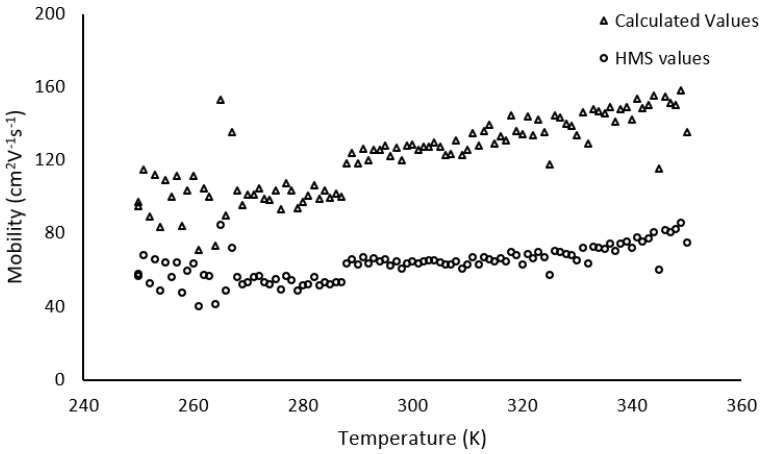

Figure 3.6: Mobility versus temperature for H-terminated diamond for data output by HMS-5000 System software and data analyzed using ASTM standards [28]

about twice as much. For both the datasets mobility increases with temperature, which is a strong indication that ionized impurity scattering is the dominant scattering mechanism in this temperature range of 250 K to 350 K. Fig 3.7 shows log of mobility versus log of temperature data-points for Calculated (ASTM) data set. Two trendlines are drawn for the dataset. The one in blue has high R^2 value of 0.95, and shows that $\mu \, a \, T^{0.86}$. The trendline in red has much lower R^2 value at 0.42, but goes through more data points. Thus, if the scatter in the data set, especially at lower temperature region, is to be reduced, the red trendline might be more fitting for the dataset. The red trendline gives $\mu \; a \; T^{\frac{3}{2}}$. Either way, mobility proportional to positive power (ideally, 3/2) for temperature range of 250 K to 350 K indicates that for this temperature range, the most dominant scattering mechanism is ionized impurity scattering [30] [31].

Carrier concentration of $2.97 \times 10^{11} \; cm^{-2}$ was obtained at 300 K assuming

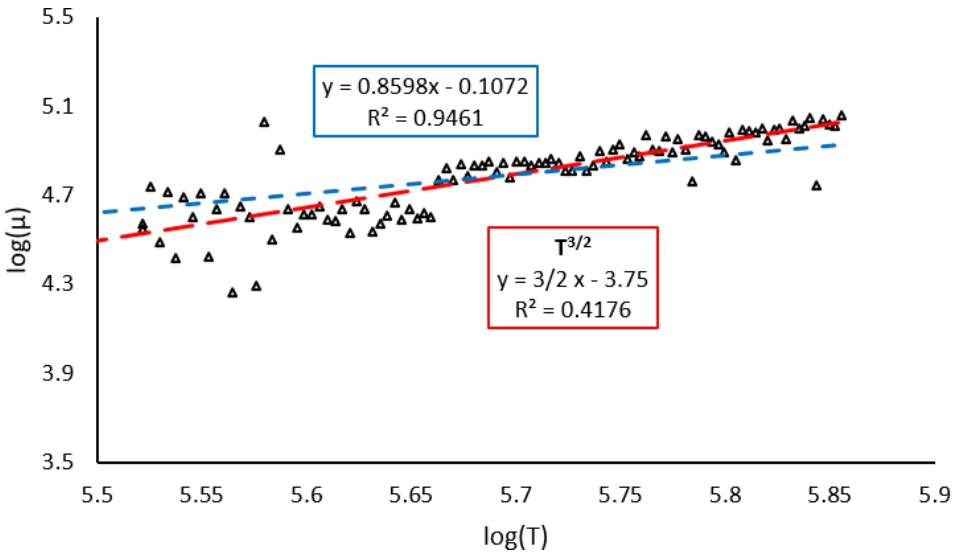

Figure 3.7: Mobility versus temperature for H-terminated diamond for data output using ASTM standards [28] and trendlines to determine $\mu$and T relationship

that the hall proportionality constant (r) is 1. Verona et. al. reported carrier concentration of 9.50 $\times 10^{12}$ cm^{-2} which is higher than 1 order of magnitude [14]. One possible explanation for this difference is that less carriers are activated for H-terminated substrate here since the sheet resistance in this work 32.4 kΩ/sq which is about 3 times greater than that reported by Verona et. al. (10.5 kΩ/sq). The higher resistance is due to lower surface coverage of hydrogen in the diamond sample in this work compared to the sample used by Verona et. al. Garrido et al. observed decrease in carrier concentration of H-terminated diamond after annealing steps at high temperatures ≥ 500 K (226°C) [27]. Carrier concentration was reduced from 9 $\times 10^{12}$ cm^{-2} to 9 $\times 10^{11}$ cm^{-2} after two annealing steps. Hence, annealing step to obtain linear I-V behavior could have led to the desorption of some surface hydrogen, reducing the total carrier concentration.

Sheet carrier concentration for H-terminated diamond increases with increasing temperature in 250 K to 350 K range, as shown in Fig 3.8 . This is not characteristic of 2DHG, which is what is expected to form near H-terminated surface because of NEA and surface transfer dopants. Sheet carrier concentration was found to be temperature independent for H-terminated diamond substrates by Hayashi et al. [32]. The temperature independent behavior is expected for carrier transport in 2D inversion layers [27]. Garrido et al. reported this temperature independence as well for H-terminated diamond substrates; however, upon annealing the H-terminated substrates at 500 K (226°C), they observed a decrease in carrier concentration with decreasing temperature. Fig 3.8 shows about 2 orders of magnitude change in carrier concentration over 250-350 K temperature range. In contrast, Garrido et al. reported less than one order of magnitude change over 100-400 K range. The stronger temperature dependence in this work could be because of the higher annealing temperature (550 °C) than that by Garrido et al. Furthermore, the deviation could also be because, in addition to 2DHG conduction channel, H-terminated diamond also has bulk conduction channel, and may have conduction channel facilitated by defects such as unintentional impurity atoms, dislocations, etc. Variable magnetic field and temperature Hall measurements can be carried out to determine effects of different conduction mechanisms [33]. Furthermore, mobility is expected to decrease with increasing carrier concentration because of increase in ionized impurity scattering. However, the amount of scattering is also affected by the interaction time between carriers and impurities [31]. The interaction time increases with temperature, so the amount of scattering decreases, leading to increase

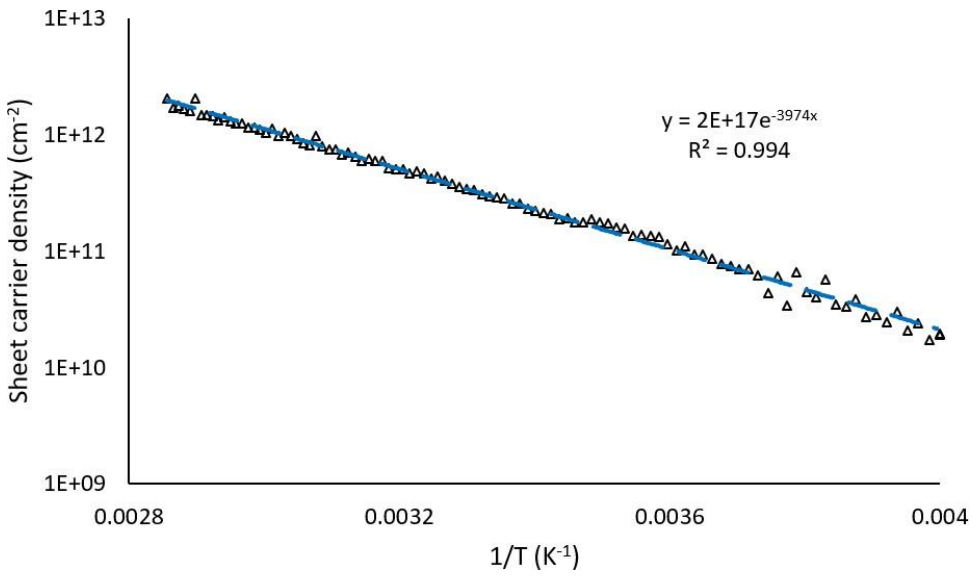

Figure 3.8: Sheet carrier density versus reciprocal temperature for H-terminated diamond for data output using ASTM standards [28]

in mobility with increasing temperature, which was observed in this case.

3.2.2 Delta doped diamond

Sample S20 which has the heavily boron-doped delta layer buried about 12 nm from the surface was prepared for Hall measurements as outlined in section 2.3.4. First, current-voltage measurements were performed to determine whether or not linear behavior was obtained. The I-V profile was not linear near room temperature as shown in fig 3.9. Hall measurements was not performed since reliable Hall measurement requires formation of good ohmic contacts.

The sample was de-mounted and prepared again for Hall measurements, only this time an annealing step was added after metal deposition to help form Ohmic contacts. RTA-600 was used to anneal the sample at 500°C for 5 minutes in N_2

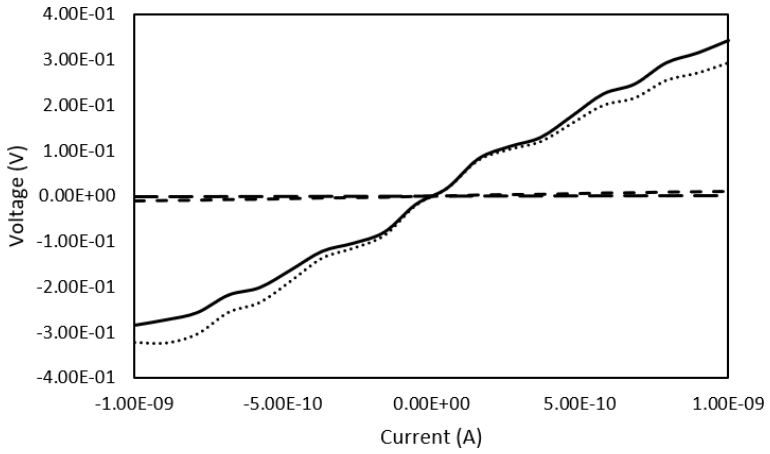

Figure 3.9: Pre-anneal I-V curves for delta-doped diamond at 288 K substrate temperature

environment. IV profile of the annleaned sample was measured again at 288 K. The annealing step led to almost perfectly linear I-V behavior, as shown in fig 3.10. There was variation in voltage response of the different pairs of contacts. This may be the result of non-uniformity in the substrate because of non-uniform delta-layer doping, or unintentional impurities. I-V profile was also measured after annealing at lower substrate temperatures. Fig 3.11 shows linear I-V behavior at substrate temperature of 200 K. At 200 K, the voltage response is about an order of magnitude higher than that at 288 K for the same applied current. This means that resistivity of the substrate must have increased at lower temperature.

Hall measurements were performed for each temperature step in the range from 210 K to 350 K. Resistivity calculations, as outlined in section 2.3.2, revealed that there were large random fluctuations in measured voltage data in the temperature range of 264 K to 292 K. Thus, data points for 264 K to 292 K temperature range

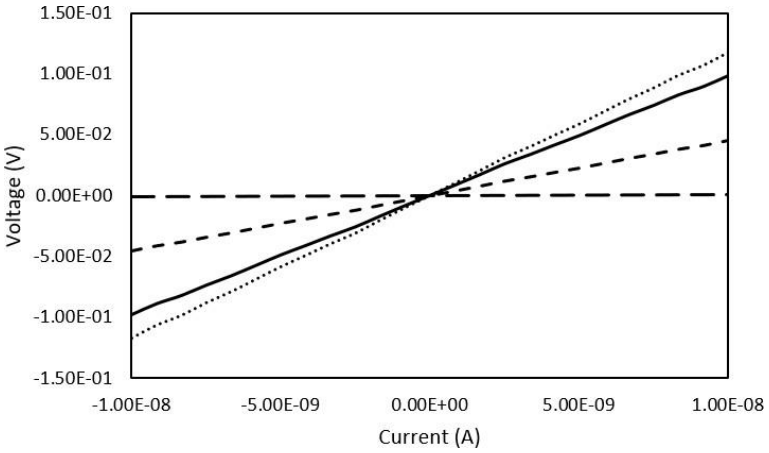

Figure 3.10: I-V curves at 288 K substrate temperature for delta-doped diamond annleaned at 500°C for 5 minutes

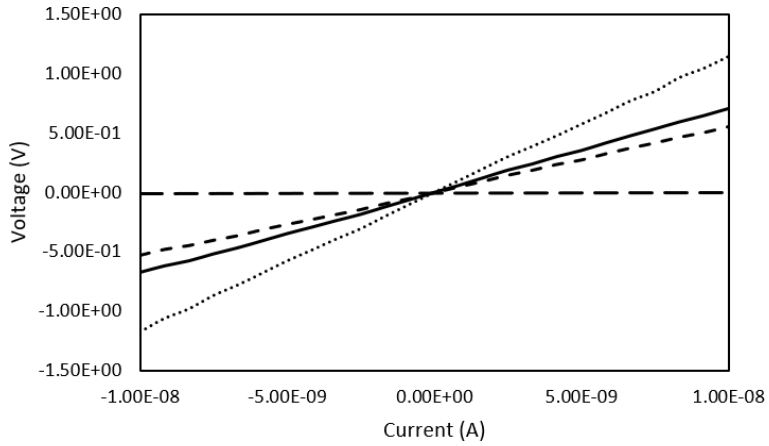

Figure 3.11: I-V curves at 200 K substrate temperature for delta-doped diamond annleaned at 500°C for 5 minutes

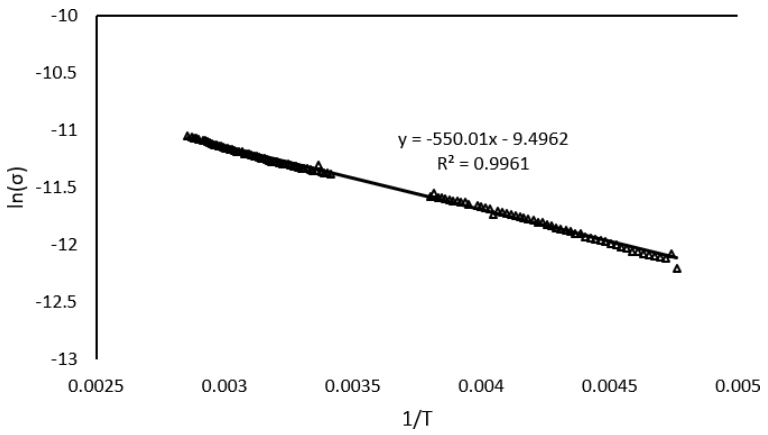

Figure 3.12: Natural logarithm of conductivity versus reciprocal temperature for delta-doped diamond for data Hall data analyzed using ASTM standards [28] along with a linear trendline

were ignored.

Resistivity of $8.4 \times 10^4\,\Omega - cm$ was obtained at 300 K. Fig 3.12 shows temperature dependence of conductivity in the form of log of conductivity versus reciprocal temperature. Using the value for slope in equation 2.18, the activation energy was calculated to be 94.8 meV. This is much lower than the acceptor level of 0.37 eV for boron. However, for high impurity concentration levels, Inushima et al. report conduction through hopping mechanism using excited level of boron [34]. The combination of the excited level of boron and optical phonons forms an impurity band through which carriers can move [35]. This manifests as a trap level between 50 and 70 meV above the valance band at the interface between heavily doped and low doped regions [34]. Activation energy of 94.8 meV obtained here is only slightly above this.

Calculation of hall coefficients showed large differences between two diagonal

hall coefficients for the same temperature. For the temperature range tested, the average hall coefficient randomly fluctuated between positive and negative value. Thus, the results show mixed carrier conduction for the bulk, instead of just conduction through holes due to the delta layer. This also meant that the carrier concentration and mobility data had a lot of variability, so much so that extraction of any trend was not possible. Even with large variability, most of the data points for mobility fell below 15 $cm^2 V^{-1} s^{-1}$. Likewise, sheet carrier density values were between 10^{10} cm^{-2} and 10^{13} cm^{-2} for both positive and negative carrier types, with a weak negative slope for sheet carrier density versus reciprocal temperature.

Double delta-doped sample was also probed using the Van der Pauw configuration. I-V measurements were conducted to make sure that there was linear behavior. Once linear I-V behavior was ensured, Hall measurements were performed for temperature range of 125 K to 350 K at input current of 0.5 mA. Measurement at temperature as low as 125 K was possible in the HMS-5000 System for double delta doped diamond because of its much lower resistivity than that of H-terminated or single delta-doped diamond. This was expected because of high doping density of 4×10^{21} cm^{-2} right at the surface. Fig 3.13 shows log of conductivity versus reciprocal temperature. A linear trendline was drawn for part of the data set at higher temperature end, as it gives a linear behavior. The slope thus extracted yielded an activation energy of 53 meV. This is slightly lower than the activation energy of 94 meV for single delta-doped diamond, but falls within the trap level of 50 and 70 meV observed by Inushima et al due to hopping conductivity [34]. Hence, conduction in double delta-doped diamond is due to hopping mechanism.

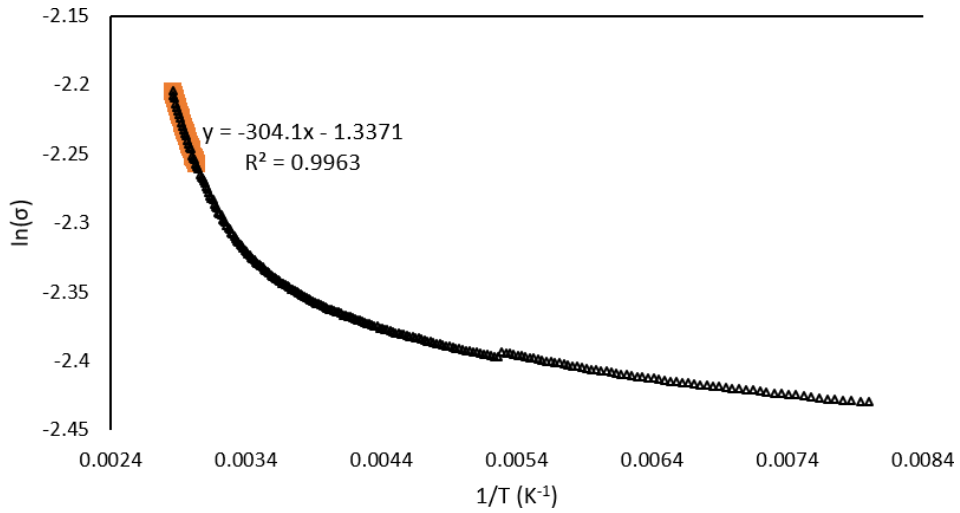

Figure 3.13: Natural logarithm of conductivity versus reciprocal temperature for double delta-doped diamond, along with a linear trendline for the highligted data-points

At temperature points below 252 K, however, there were fluctuations in hall coefficients similar to that for single delta-doped diamond. The hall coefficients fluctuated between positive and negative values below 252 K, but were always positive for temperatures above 252 K. Thus, above 252 K, conduction occurs predominantly due to p-type carriers, whereas below this temperature, conduction occurs due to mixed carriers. At 300 K, resistivity of 10.1 $\Omega - cm$, mobility of 11.4 $cm^2 V^{-1} s^{-1}$, and sheet carrier density of 5.4×10^{16} cm^{-2} was obtained. Fig 3.14 shows mobility versus temperature relation. The highlighted linear part of the data set was used to calculate the following dependence of mobility on temperature: $\mu \; a \; T^{12}$. This dependency is much greater than the usual $T^{3/2}$ relationship for ionized impurity scattering. The mobility values fluctuate below 252 K as expected because of fluctuating hall coefficients at those temperature points.

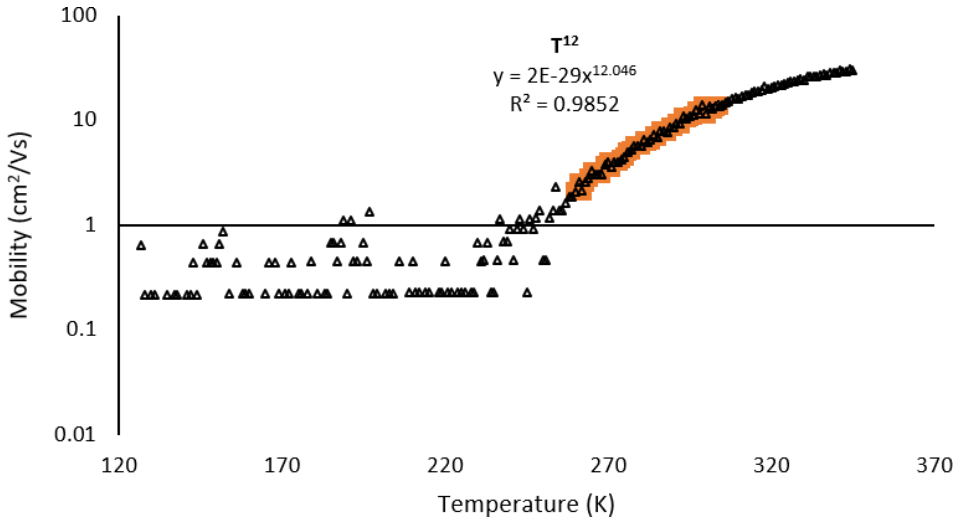

Figure 3.14: Mobility versus temperature for double delta-doped diamond and trend-line for the highlighted linear part of the data set to determine μ and T relationship

Fig 3.15 shows bulk carrier concentration versus reciprocal temperature for temperatures above 252 K. Again, this range was selected due to large spread in data below 252 K. Carrier concentration decreases with increasing temperature for 252 K to 350 K. The highest bulk carrier concentration in this range is $5.1 \times 10^{17}\ cm^{-3}$, thus, sheet carrier concentration must be below this number. However, boron concentration is in excess of $1 \times 10^{21}\ cm^{-2}$ for both the surface and sub-surface delta layers. The significantly lower value for carrier concentration could be because of partial ionization of boron impurities. Also, number of ionized impurities should increase with increasing temperature as there is more thermal energy, which is opposite to what is observed in this case. This means that there must be increasing compensation of p-type carriers in this temperature range.

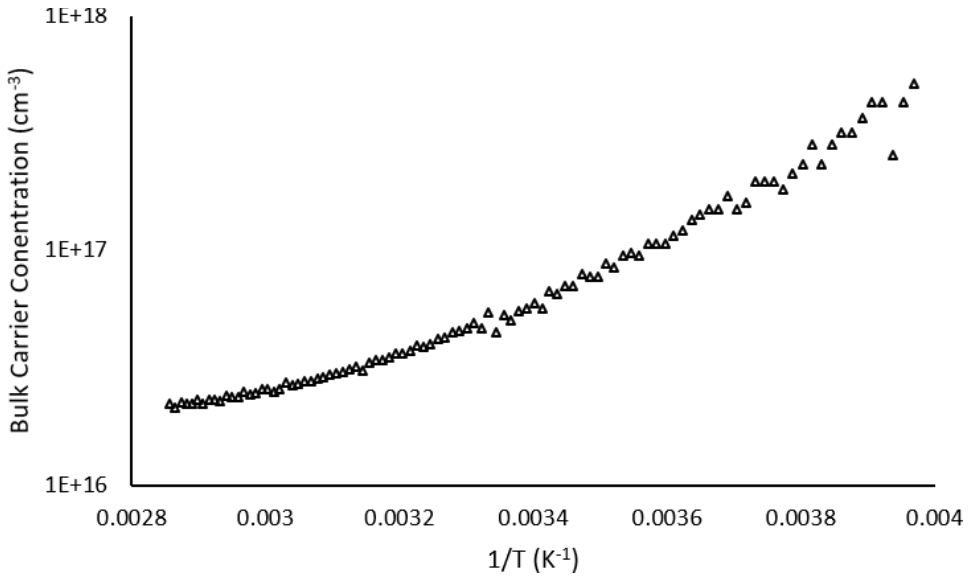

Figure 3.15: Bulk carrier density versus reciprocal temperature for double delta-doped diamond

3.3 Post-irradiation Hall Measurement

Measurement of I-V characteristics after proton irradiation showed degradation of Ohmic behavior for both H-terminated and delta doped diamonds. Because of this, the processed data showed more scatter in the range than that for pre-radiation case. Hall measurements were taken in the range of 288 K to 350 K. Hall measurements at lower temperatures were increasingly difficult because of the increase in resistivity with decreasing temperature. This is because it was harder to measure the higher voltage differences because of HMS-5000 System limitation.

3.3.1 H-terminated diamond

Following irradiation with protons, H-terminated diamond showed degradation of ohmic contacts as seen from the deviation from linear I-V behavior in fig 3.16(a). This caused there to be greater error in the calculated data for resistivity and hall coefficient, resulting in greater scatter in temperature dependent resistivity, mobility and carrier concentration datasets. Thus, to get more relaible temperature dependence datasets, the contacts were annealed at 550°C for 1 minute. Post-anneal measurements, shown in fig 3.16(b), showed improvement in linear behavior. But, at input current in microAmpere regime, the I-V behavior was still poor. I-V measurements taken at input current in nanoAmpere regime, however, show far better linear relationship, as evidenced by fig 3.17. At this input current domain, annealing at 550°C for a minute leads to dramatic improvement in linear I-V behavior. Also seen is that the voltage response for the same input current decreased by an order of magnitude as a result of annealing.

Hall measurements were performed for both post-irradiation as-is and post-irradiation annealed cases at input current of 1 nA. Quality of ohmic contact had a direct effect on resistivity calculations. Fig 3.18 shows comparision of temperature dependent resistivity values between pre-radiation, post-radiation, and post-radiation annealed cases. The dramatic increase in post-radiation resistivity values result from error in resistivity calculation due to non-linear I-V behavior. In contrast, the post-irradiation annealed resistivity values are slightly greater than pre-irradiation values. This increase in resistivity could be due to damage caused

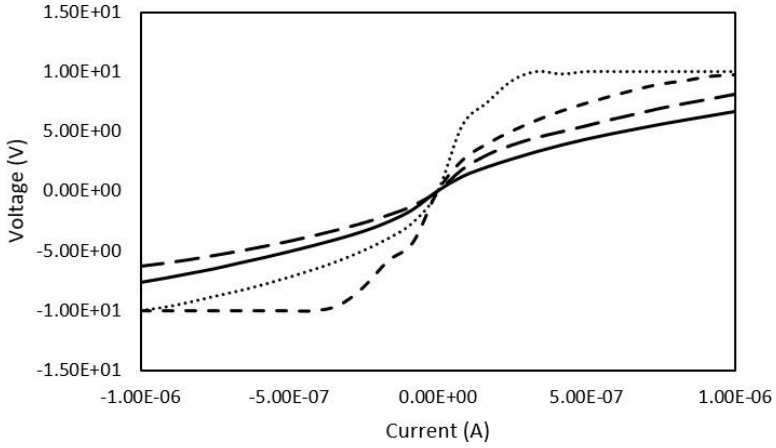

(a)

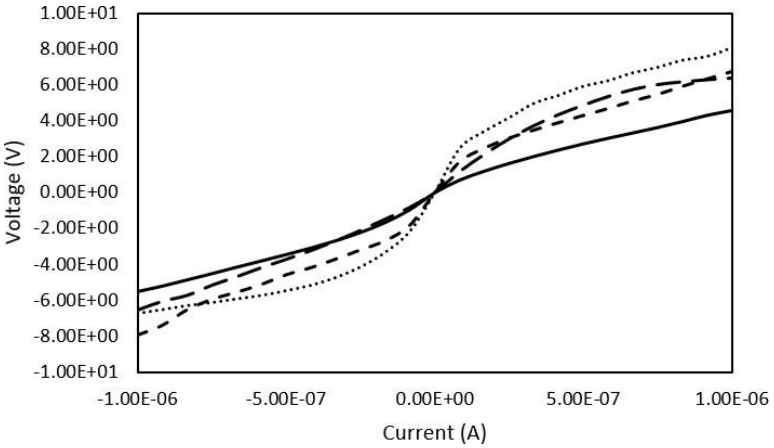

(b)

Figure 3.16: I-V curves at 288 K substrate temperature for H-terminated diamond after proton irradiation (a) as-is (b) after annealing at 550°C for 1 minute

by irradiation.

Fig 3.19 shows natural log of conductivity versus reciprocal temperature graphs for post-irradiation as-is and post-irradiation annealed cases. Activation energy (E_g) of 0.639 eV was obtained from the slope of the dataset for post-irradiation as-is case, a decrease from 0.76 eV for pre-irradiation case. Activation energy (E_g) for post-irradiation annealed case was even lower at 0.407 eV. Degradation of linear I-V behavior may have contributed to the deviation from activation energy of pre-

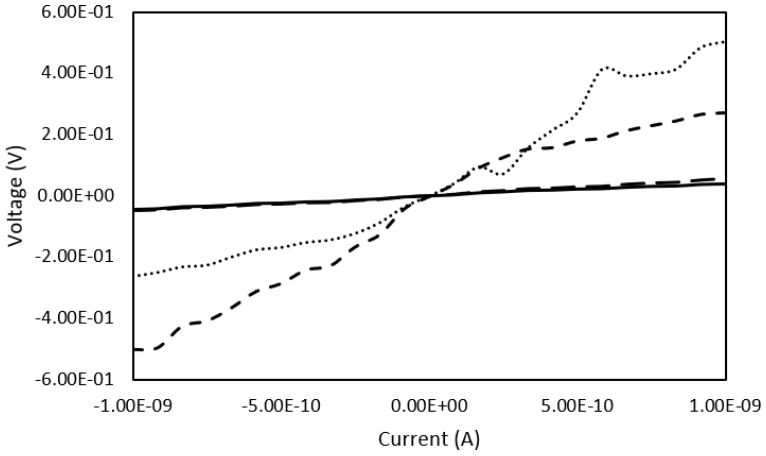

(a)

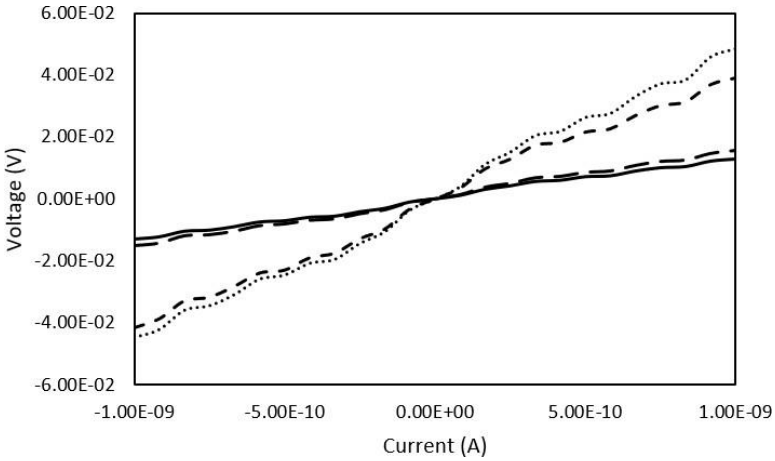

(b)

Figure 3.17: I-V curves at 288 K substrate temperature for H-terminated diamond after proton irradiation for nanoAmpere input current regime (a) as-is (b) after annealing at 550°C for 1 minute

irradiation case. However, this deviation seems more strongly correlated to radiation damage. This is because when ohmic behavior was improved by post-irradiation annealing process, the difference in activation energy between pre-irradiation and post-irradiation annealed cases became even more pronounced than that between pre-irradiation and post-irradiation as-is case. Thus, proton irradiation introduced trap states, which facilitated the electrical conduction.

Diagonal hall coefficients for each temperature point calculated using equations

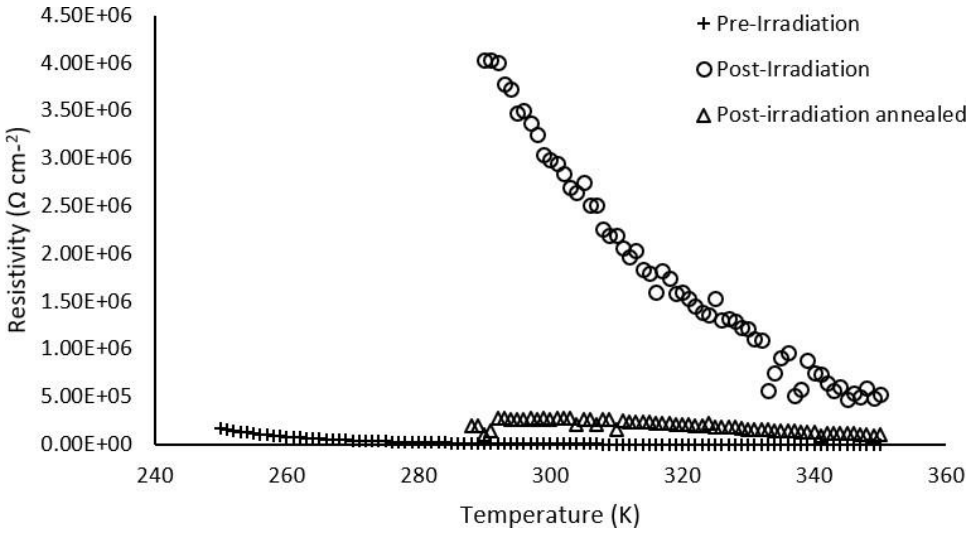

Figure 3.18: Resistivity versus temperature for H-terminated diamond before and after proton irradiation

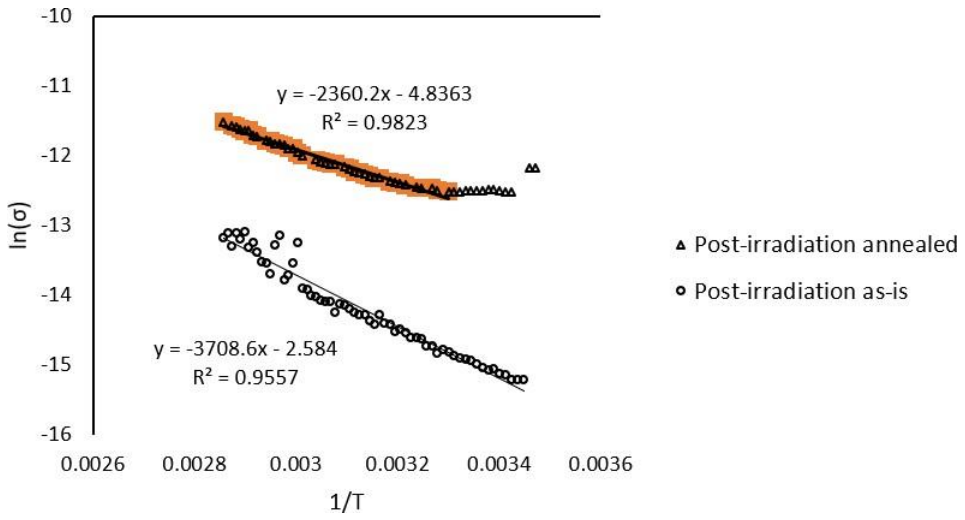

Figure 3.19: Natural log of conductivity versus reciprocal temperature for H-terminated diamond after proton irradiation as-is and after annealing at 550°C for 1 minute

2.8 and 2.9 had a lot of variation. This is the effect of sample inhomogeniety caused by proton irradiaiton. Furthermore, for some temperature points, the two diagonal hall coefficients had opposite signs. This means that conduction in H-terminated diamond post-irradiation is due to mixed carriers, rather than just a single carrier type. Moreover, this large spread in hall coefficient data set resulted in large spread in mobility and carrier concentration data sets. Thus, no trend for mobility and carrier concentration with respect to temperature could be identified. Even with this spread, thirty-nine out of sixty-three total mobility data points in the temperature range of 288 K to 350 K for post-irradiation annealed case had values less than 15 $cm^2 V^{-1} s^{-1}$. Likewise, sheet carrier concentration data set for post-irradiation as-is case was in 10^7 to 10^9 cm^{-2} range, with most data points in 10^8 cm^{-2} regime. And for post-irradiation annealed case, sheet concentration data set was in 10^9 to 10^{11} cm^{-2} range.

3.3.2 Delta doped diamond

After proton-irradiation, delta-doped diamond showed degradation in ohmic contacts similar to that for H-terminated diamond. Fig 3.20(a) shows this deviation from linear behavior. Also, for the same input current, voltage difference increased by an order of magnitude than for the pre-irradiation case. However, after annealing the contacts at 600°C for 1 minute, the I-V behavior was linear again, as seen in fig 3.20(b).

Hall measurements were taken for post-irradiation as-is case at input current

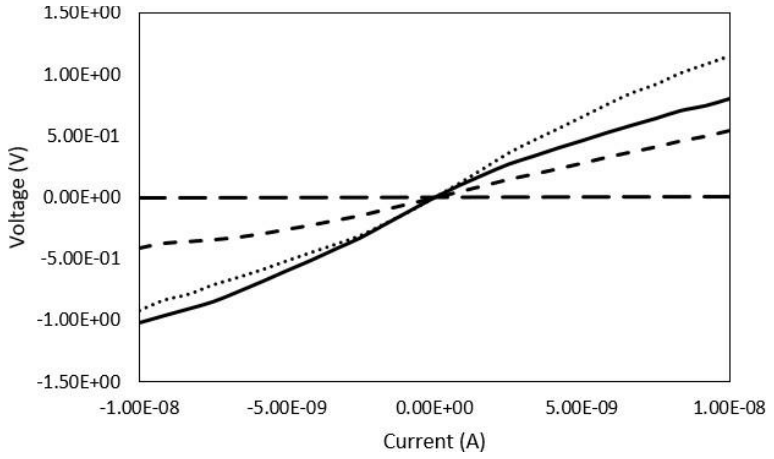

(a)

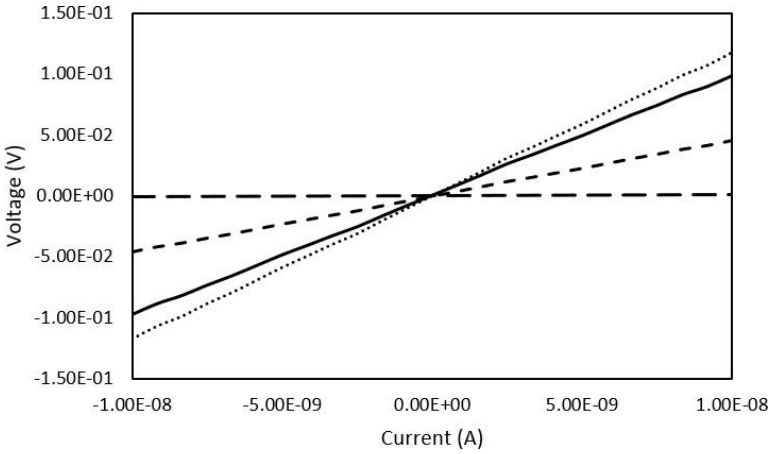

(b)

Figure 3.20: I-V curves at 288 K substrate temperature for delta-doped diamond after proton irradiation (a) as-is (b) after annealing at 600°C for 1 minute

of 1 nA to minimize error. For post-irradiation annealed case, measurements were taken at 10 nA input current as was done for pre-irradiation case. The degradation of ohmic behavior due to proton irradiation resulted in increase in resistivity values by an order of magnitude. This effect subsided once the contacts were annealed at 600°C for 1 minute. The resistivity values for post-irradiation annealed case matched very closely to that of pre-irradiation case, especially at higher temperatures. Fig 3.21 shows the difference in resistivity values for all three cases. This behavior

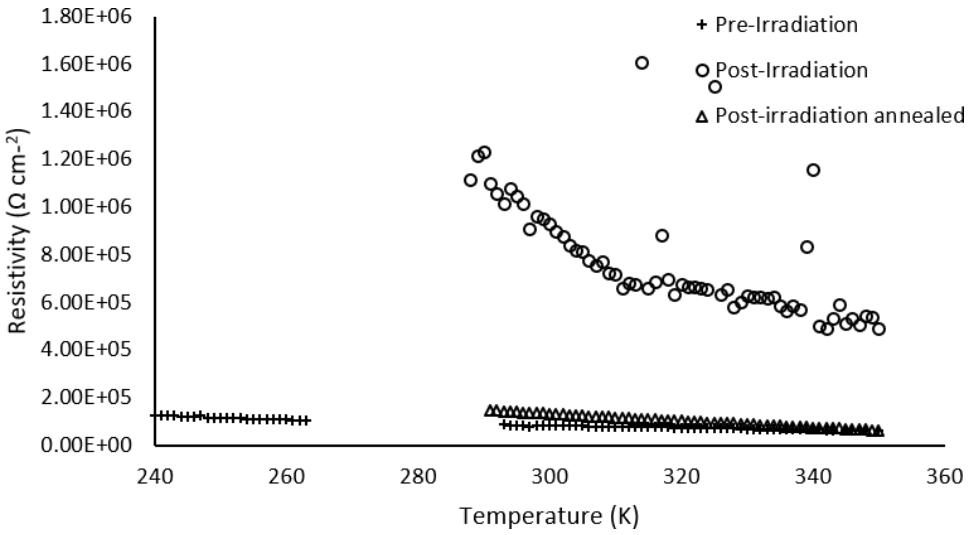

Figure 3.21: Resistivity versus temperature for delta-doped diamond before and after proton irradiation

for resistivity was also exhibited by H-terminated diamond. Hence, the dramatic increase in resistivity is a result of degradation of ohmic contacts due to proton irradiation. When ohmic contacts were annealed to obtain linear I-V behavior, resistivity values were only slightly higher than for pre-irradiation case.

Fig 3.22 shows natural log of conductivity versus reciprocal temperature graphs for post-irradiation as-is and post-irradiation annealed cases. For both the data sets, trendlines are drawn for the linear parts to obtain information about activation energy. The data points making up the linear region are highlighted for both data sets. Pre-irradiation case, which has more spread in the data set, gives activation energy of 0.366 eV. Post-irradiation case with far less spread due to linearity in I-V measurements gives activation energy of 0.356 eV, very close to that for post-irradiation as-is case. The activation energy values are close to boron acceptor level

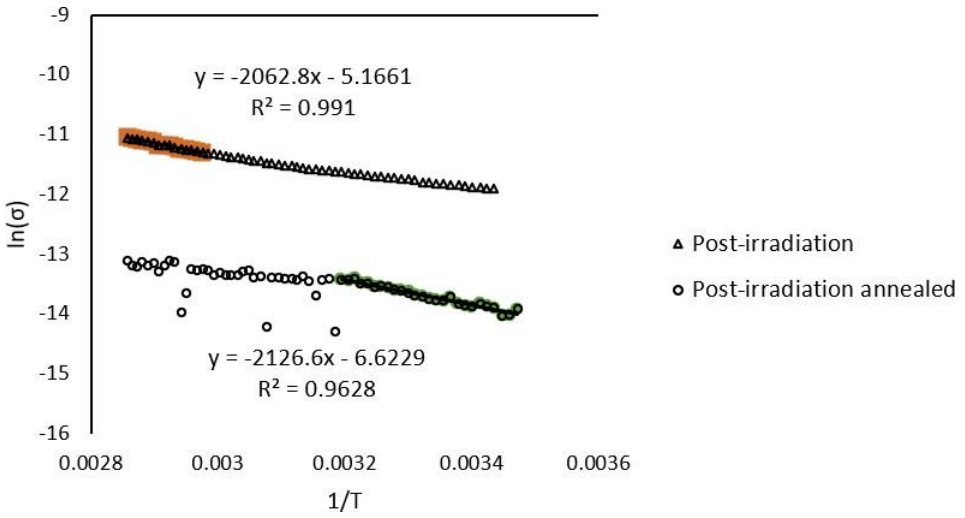

Figure 3.22: Natural log of conductivity versus reciprocal temperature for delta-doped diamond after proton irradiation as-is and after annealing at 600°C for 1 minute

of 0.37 eV. The post-irradiation activation energies are markedly higher than 0.0948 eV for the pre-irradiation case. This means that conduction through the valence band is dominant after irradiation. This could be due to disruption of the shallow level of 94.8 meV.

Hall coefficients for both post-irradiation as-is and post-irradiation annealed cases showed similar characteristics. There was high fluctuation in the hall coefficients to the extent that sometimes the diagonal coefficients for the same temperature point had opposite signs. This means that there was mixed type of carriers. Also, as a result of the spread in hall coeffcients, calculated mobility and sheet concentration values had a large spread. This was especially true for post-irradiation as-is case. For post-irradiation annealed case, while the highest mobility value was 608.5 $cm^2 V^{-1} s^{-1}$, thirty-eight out of sixty total data points in the tested temper-

ature range of 291 K to 350 K yielded mobility values less than 10 $cm^2 V^{-1} s^{-1}$. Thus, activation energy for conduction increased, and carrier concentration and hall mobility decreased after proton irradiation.

3.4 Device Simulation

Device simulation was performed to understand the post-irradiation degradation of output current from device point of view. Using the quadratic model and constant mobility assumption, drain current as a function of source voltage was modeled. The gate voltage used was from 5 V to -5 V for threshold voltage assumed to be 5.1 V. Mobility values obtained from Hall measurements (listed in table 3.1) was used in the model. For H-terminated diamond, Al_2O_3 is used as gate oxide, whereas for delta-doped diamond, the intrinsic cap layer serves this purpose. Fig 3.23 and 3.24 show pre- and post- irradiation drain current output versus source voltage for FETs based on H-terminated and delta doped diamond respectively. Maximum drain current (I_D) values are also listed in table 3.1 for each case for gate voltage of -5 V. For -5 V gate bias, the maximum drain current decreased by 95% for H-terminated diamond post irradiation. And, for delta-doped diamond, the maximum drain current decreased by 37%.

Table 3.1: Parameters used in quadratic constant mobility model for MOSFET IV characteristics

	H-terminated		Delta-doped	
Dielectric material Dielectric constant Dielectric layer depth (nm)	Al_2O_3 9 25		Intrinsic diamond 5.7 12	
Mobility at 300 K ($cm^2V^{-1}s^{-1}$)	128.3	6.49	2.92	1.84
Max. drain current at V_g = -5V (mA/mm)	695	35.15	20.87	13.15

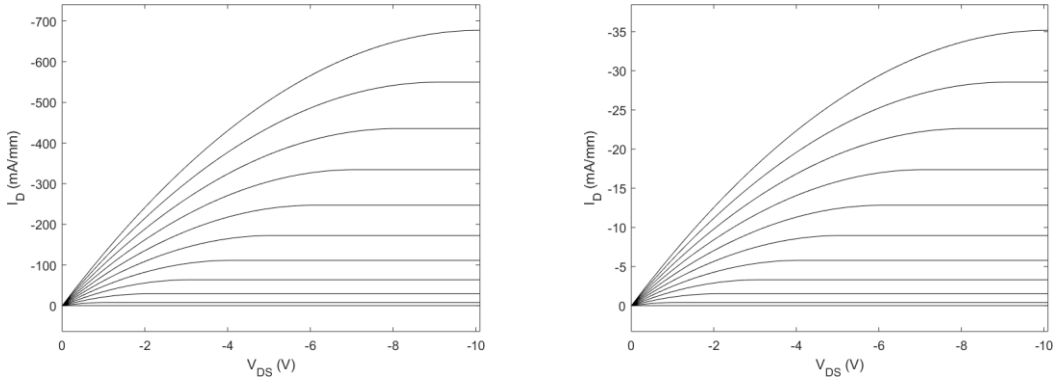

(a) (b)

Figure 3.23: I-V characteristics for H-terminated diamond (a) pre- and (b) post-irradiation with protons

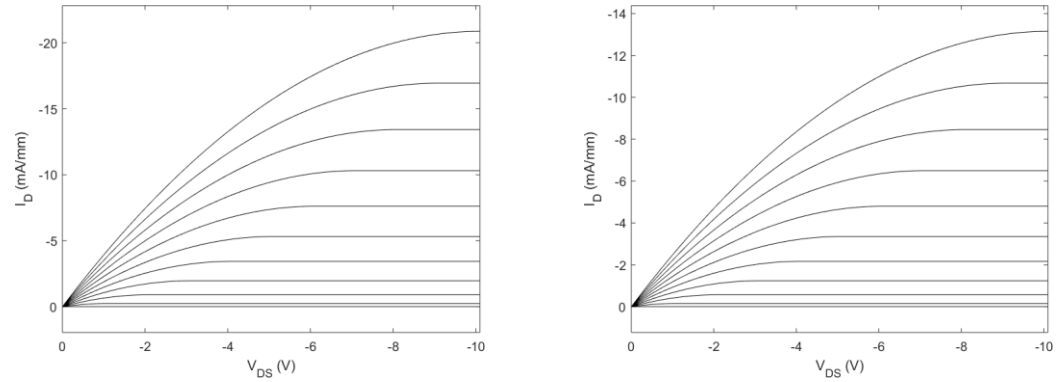

(a) (b)

Figure 3.24: I-V characteristics for delta-doped diamond (a) pre- and (b) post-irradiation with protons

Chapter 4: Conclusions and Future Directions

4.1 Conclusions

Due to high thermal conductivity, mechanical robustness and ultra-wide bandgap, diamond shows great promise as material for high frequency, high-power device applications. Also, due to high binding energy of carbon atoms in diamond, it is predicted to be radiation hard. Radiation hardness would allow diamond based sensors and devices to be used in harsh environments such as outer-space, nuclear reactors, and the Large Hadron Collider, etc. This work explored radiation hardness of diamond from device point of view.

As such, the diamonds tested had conducting channel activated much below the ultra wide bandgap energy of diamond. This was possible in two ways: (1) terminating HPHT diamond surface with hydrogen, and (2) incorporating heavily boron doped delta layer tens of nanometers underneath the top surface.

FETs were fabricated on H-terminated substrates. Blanket Au layer was deposited, then patterened into mesas, and subjected to O_2 plasma to remove H-termination, isolating the devices. More patterning was done to form Ohmic contacts. Finally, gate dielectric, Al_2O_3, was deposited by ALD, followed by e-beam and liftoff processes to deposit Al gate on top. The FETs were subjected to gamma

irradiation from a total dose of 1 kRad to 26.3 MRad. At low dose up to 100 kRad, the FETs showed slight decrease in drain current output, threshold voltage, and maximum transconductance. This could be due to the formation of defects which act as scattering centers. However, vacancies formed Campbell and Mainwood's simulation shows that very few i.e. ≤ 0.09 vacancies/gamma per cm are formed in diamond by gamma irradiation of 1 and 2 MeV [23]. Thus, further research is necessary to determine the cause. In contrast, after high dose ≥ 13.6 MRad gamma irradiation, the drain current output increased sigificantly. Gamma irradiation can form trap states by introducing defects, which could result in enhanced hoping conductivity that is responsible for higher output drain current. However, threshold voltage also increased significantly, while gate leakage current remained unchanged.

Radiation hardness of diamond was also evaluated for proton irradiation. A cyclotron was used to bombard the samples with 152 keV protons at fluence of $1.03 \times 10^{12}\ cm^{-2}$. This time, bare substrates of H-terminated and delta-doped diamond were used. Hall measurements using the Van der Pauw configuration were performed to evaluate changes in transport properties. Diamond substrates were too small, however, for the available Hall measurement system, HMS-5000, to probe them directly. An alternative approach was designed to get around this size limitation. Insulating pieces of SiO_2 substrate were patterned with Cr/Au contact pads in the corners. The small diamond substrates also with Cr/Au contact pads in the corners were glued to these bigger SiO_2 substrate using LOR7B resist. This was followed by wire-bonding to join Cr/Au pads on the diamond substrates with Cr/Au pads on the SiO_2 substrates. Probes of HMS-5000 System could then be

dropped on the Cr/Au pads on the SiO_2 substrate to perform Hall measurements on the diamond glued to it.

Appropriate input current was selected for each substrate before and after proton irradiation to ensure measurements in linear I-V region. At 300 K, H-terminated diamond showed resistivity of $8.21 \times 10^3\ \Omega - cm$, carrier concentration of $2.97 \times 10^{11}\ cm^{-2}$, and hall mobility of $128.3\ cm^2 V^{-1} s^{-1}$. Conduction by p-type carriers and activation energy of 0.76 eV was obtained. Also, mobility increased with temperature closely matching the relationship with temperature of $\mu\ a\ T^{\frac{3}{2}}$, which is widely accepted to be due to ionized impurity scattering. After proton irradiation, Hall measurements showed significant differences. At 300 K, sheet resistivity increased to $2.69 \times 10^5\ \Omega - cm$, carrier concentration decreased to $1.8 \times 10^{11}\ cm^{-2}$, and mobility also decreased to $6.49\ cm^2 V^{-1} s^{-1}$. Hall coefficient showed fluctuation between positive and negative sign, indicating mixed carrier conduction. Activation energy decreased to 0.407 eV, indicating formation of a new trap level due to proton irradiation.

Likewise, for delta-doped diamond, resistivity of $8.37 \times 10^4\ \Omega - cm$, carrier concentration of $1.27 \times 10^{12}\ cm^{-2}$, and mobility of $2.92\ cm^2 V^{-1} s^{-1}$ was obtained at 300 K. Hall coefficients again showed mixed carrier conduction. Activation energy of 94.7 meV was obtained, which is close to the expected activation energy for hopping conduction reported by Inushima et al [34]. After proton irradiation, at 300 K, resistivity increased to $1.33 \times 10^5\ \Omega - cm$, sheet carrier concentration was the same at $1.27 \times 10^{12}\ cm^{-2}$, and mobility decreased to $1.84\ cm^2 V^{-1} s^{-1}$. Hall coefficients indicated mixed carrier conduction. Activation energy increased significantly to

0.356 eV, which is close to the boron acceptor level, indicating disruption of the shallow trap state.

Simulation of drain current versus source voltage showed degradation of maximum drain current output by 95% for H-terminated diamond post proton irradiation. Similarly, for delta-doped diamond, maximum drain current output decreased by 37% after proton-irradiation.

4.2 Future Directions

Based on the results of this work, several topics can be investigated to continue the advancement of knowledge in diamond based devices. First and foremost, better controls must be implemented for more reliable results through improvement in ohmic contacts, monitoring surface hydrogen coverage, and fabricating smaller structures, thus allowing less variability, for Hall measurements. A more robust and reliable contact scheme must be developed to good obtain ohmic behavior and avoid delamination of contacts. This can be done through alloyed contact processing for different metal combinations. To explore different contact schemes as well as measure contact resistance, and sheet resistivity, circular transfer length method (CTLM) pattern has already been prepared to be patterned using electron-beam direct write procedure. If successful, this would significantly improve the reliability of measurements of FETs as well as that of Hall measurements. Likewise, because hydrogen termination is unstable at high temperatures, surface coverage of diamond with hydrogen should be mapped for the entire surface using Micro-Raman spec-

troscopy. This would also be useful to monitor homogeniety of H-terminated samples, which is crucial for accuracy of Hall coefficient calculation. To ensure less variability, Hall measurements can be performed using Hall bar configuration fabricated at a scale of about 100 microns. Also, variable magnetic field Hall measurement can be used to determine contributions from bulk and 2D conduction separately. Furthermore, higher dose gamma irradiation and additional proton fluences should be used in addition to different defect characterization techniques such as deep level transient spectroscopy (DLTS), capacitance-voltage-temperature (C-V-T), photocapacitance, and deep level optical spectroscopy (DLOS), etc. to understand the fundamental effects of radiation on p-channel diamond substrates and devices.

Bibliography

[1] D. I. Shahin, K. K. Kovi, A. Thapa, Y. Lu, J. E. Butler, and A. Christou, "Radiation Effects in Diamond Electronics with 2-D Transport Channels Comparison with GaN eHEMTs" *GOMACTech*, (2019).

[2] D.I. Shahin, K.K. Kovi, A. Thapa, Y. Lu, I. Ponomarev, J.E. Butler, A. Christou, "Fabrication and Characterization of Diamond FETs with 2D Conducting Channels," *2018 International Workshop on Compound Semiconductor Manufacturing Technology (CS-MANTECH)* 14.11, (2018).

[3] W. D. Callister, and D. G. Rethwisch, "Fundamentals of Materials Science and Engineering: an Integrated Approach." (Wiley, USA, 2012). Chap. 3.

[4] K. E. Spear, and J. P. Dismukes, (Eds.). "Synthetic diamond: emerging CVD science and technology." **25** (John Wiley & Sons, 1994), Chap. 1.

[5] C. A. Klein, "Diamond windows for IR applications in adverse environments." *Diamond and Related Materials* **2**(5-7), 1024 (1993).

[6] C. A. Klein, "Diamond windows and domes: flexural strength and thermal shock." *Diamond and related materials* **11**(2), 218 (2002).

[7] P. W. May, "The new diamond age?." *Science* **319**(5869), 1490 (2008).

[8] J. Y. Tsao et. al., "Ultrawide-bandgap semiconductors: Research opportunities and challenges" *Advanced Electronic Materials* **4**, 1600501 (2018).

[9] R. J. Kaplar, A. A. Allerman, A. M. Armstrong, M. H. Crawford, J. R. Dickerson, A. J. Fischer, A. G. Baca, and E. A. Douglas, "Ultra-wide-bandgap AlGaN power electronic devices." *ECS Journal of Solid State Science and Technology* **6**(2), Q3061 (2017).

[10] P.-C. Chao, K. Chu, C. Creamer, J. Diaz, T. Yurovchak, M. Shur, R. Kallaher, C. McGray, G. D. Via, J. D. Blevins, "Low-Temperature Bonded GaN-on-Diamond HEMTs With 11 W/mm Output Power at 10 GHz" *IEEE Trans. Electron Devices* **62** (11), 3658 (2015).

[11] M. J. Tadjer, T. J. Anderson, K. D. Hobart, T. I. Feygelson, J. D. Caldwell, C. R. Eddy Jr., F. J. Kub, J. E. Butler, B. Pate, J. Melngailis, "Reduced Self-Heating in AlGaN/GaN HEMTs Using Nanocrystalline Diamond Heat-Spreading Films." *IEEE Electron Device Lett.* **33** (1), 23 (2012).

[12] K. D. Chabak, J. K. Gillespie, V. Miller, A. Crespo, J. Roussos, M. Trejo, D. E. Walker Jr., G. D. Via, G. H. Jessen, J. Wasserbauer, "Full-Wafer Characterization of AlGaN/GaN HEMTs on Free-Standing CVD Diamond Substrates." *IEEE Electron Device Lett.* **31**(2), 99 (2010).

[13] T. P. Chow, I. Omura, M. Higashiwaki, H. Kawarada, and V. Pala, "Smart power devices and ICs using GaAs and wide and extreme bandgap semiconductors." *IEEE Transactions on Electron Devices* **64**, 856 (2017).

[14] C. Verona, W. Ciccognani, S. Colangeli, E. Limiti, M. Marinelli, and G. Verona-Rinati,"Comparative investigation of surface transfer doping of hydrogen terminated diamond by high electron affinity insulators," *J. Appl. Phys.* **120**, 025104 (2016).

[15] Y. Takagi, K. Shiraishi, M. Kasu, and H. Sato, "Mechanism of hole doping into hydrogen terminated diamond by the adsorption of inorganic molecule," *Surf. Sci.* **609**, 203 (2013).

[16] C.J. Wort, and R.S. Balmer, "Diamond as an electronic material." *Materials today* **11** (1-2), 22-28 (2008).

[17] K. Hirama, H. Sato, Y. Harada, H. Yamamoto, and M. Kasu, "Diamond field-effect transistors with 1.3 A/mm drain current density by Al2O3 passivation layer." *Jpn. J. Appl. Phys.* **51** (9R), 090112 (2012).

[18] H. Kawarada, H. Tsuboi, T. Naruo, T. Yamada, D. Xu, A. Daicho, T. Saito, and A. Hiraiwa, "CH surface diamond field effect transistors for high temperature (400 C) and high voltage (500 V) operation." *Appl. Phys. Lett.* **105** (1), 013510 (2014).

[19] C. Verona, W. Ciccognani, S. Colangeli, E. Limiti, M., Marinelli, G. Verona-Rinati, E. Santoni, E., M. Angelone, M. Pillon, F. Pompili, and M. Benetti, "14.8-MeV neutron irradiation on H-terminated diamond-based MESFETs." *IEEE Electron Device Letters* **37** (12), 1597-1600 (2016).

[20] P. J. Sellin, and J. Vaitkus, "New materials for radiation hard semiconductor dectectors." *Nuclear Instruments and Methods in Physics Research Section A* **557** (2), 479-489 (2006).

[21] Mainwood, A., "Recent developments of diamond detectors for particles and UV radiation." *Semicond. Sci. Technol.* **15** (9), R55 (2000).

[22] J. Kim, S. J. Pearton, C. Fares, J. Yang, F. Ren, S. Kim, A. Y. Polyakov, "Radiation damage effects in Ga 2 O 3 materials and devices." *Journal of Materials Chemistry C* **7** (1), 10-24 (2019).

[23] B. Campbell, and A. Mainwood, "Radiation damage of diamond by electron and gamma irradiation." *phys. stat. sol. (a)* **181** (1), 99 (2000).

[24] S. J. Pearton, F. Ren, E. Patrick, M. E. Law, and A. Y. Polyakov, "Ionizing radiation damage effects on GaN devices." *ECS Journal of solid state science and technology*, **5** (2), Q35-Q60 (2016).

[25] A. Johnston, "Reliability and radiation effects in compound semiconductors." *World Scientific* (2010).

[26] C.-L. Cheng, C.-F. Chen, W.-C. Shaio, D.-S. Tsai and K.-H. Chen, "The CH stretching features on diamonds of different origins," *Diamond and Related Materials* **14**, 1455 (2005).

[27] J. A. Garrido, T. Heimbeck, and M. Stutzmann, "Temperature-dependent transport properties of hydrogen-induced diamond surface conductive channels." *Physical Review B* **71** (24), 245310 (2005).

[28] ASTM Standard F76, "Standard Test Methods for Measuring Resistivity and Hall Coefficient and Determining Hall Mobility in Single-Crystal Semiconductors," *ASTM International*, (2008).

[29] "Hall Effect Measurements - Temperature Dependence." *Warwick: Department of Physics*, 1 (2010).

[30] C. E. Nebel, "Surface transfer-doping of H-terminated diamond with adsorbates," *New Diamond Front. Carbon Technol.* **15**, 247 (2005).

[31] B. V. Zeghbroeck, "Principles of Semiconductor Devices," (2011), Chap. 2.

[32] K. Hayashi, S. Yamanaka, H. Okushi, and K. Kajimura, "Study of the effect of hydrogen on transport properties in chemical vapor deposited diamond films by Hall measurements." *Applied physics letters* **68** (3), 376-378 (1996).

[33] S. B. Lisesivdin, N. Balkan, and E. Ozbay, "A simple parallel conduction extraction method (SPCEM) for MODFETs and undoped GaN-based HEMTs," *Microelectronics Journal* **40** (3), 413 (2009).

[34] T. Inushima, T. Matsushita, S. Ohya, and H. Shiomi, "Hopping conduction via the excited states of boron in p-type diamond." *Diamond and Related Materials* **9** (3-6), 1066 (2000).

[35] T. Inushima, A. Ogasawara, T. Shiraishi, S. Ohya, S. Karasawa, and H. Shiomi, "On the properties of impurity bands generated in P-type homoepitaxial diamond." *Diamond and related materials* **7** (6), 874 (1998).

[36] D. A. Neamen, "Semiconductor Physics and Devices: Basic Principles 4th Edition." (2011).

[37] R. Velazco, P. Fouillat, and R. Reis, eds. "Radiation effects on embedded systems." Springer Science & Business Media, (2007).

[38] J. R. Srour, and J.W. Palko, "Displacement damage effects in irradiated semiconductor devices." *IEEE Transactions on Nuclear Science* **60** (3), 1740-1766 (2013).

[39] A. Ionascut-Nedelcescu, C. Carlone, A. Houdayer, H. J. Von Bardeleben, J. L. Cantin, and S. Raymond, "Radiation hardness of gallium nitride." *IEEE Transactions on Nuclear Science*, **49** (6), 2733-2738 (2002).

[40] T. Ohshima, H. Itoh, and M. Yoshikawa, "Effect of gamma-ray irradiation on the characteristics of 6H silicon carbide metal-oxide-semiconductor field effect transistor with hydrogen-annealed gate oxide." *J. Appl. Phys.* **90** (6), 3038-3041 (2001).

[41] R. Kannan, S. Krishnamurthy, C. C. Kiong, and T. B. Ibrahim, "Impact of gamma-ray irradiation on dynamic characteristics of Si and SiC power MOSFETs." *International Journal of Electrical and Computer Engineering* **9** (2), 1453 (2019).

[42] M. Kasu, K. Ueda, Y. Yamauchi, A. Tallaire, and T. Makimoto, "Diamond-based RF power transistors: Fundamentals and applications." *Diamond and Related Materials*, **16** (4-7), 1010-1015 (2007).